

## Systems Article

# Lessons Learned from two iterations of LLAMA, an Electrically Powered, Dynamic Quadruped Robot

Jay Jasper<sup>1</sup>, Ara Kourchians<sup>1</sup>, Mark Gonzalez<sup>3</sup>, Blair Emanuel<sup>1</sup>, John Nicholson<sup>4</sup>, Greg McCutcheon<sup>5</sup>, Max Austin<sup>4</sup>, Matt Kozlowski<sup>7</sup>, Emma Holmes<sup>7</sup>, Rachel Hegeman<sup>7</sup>, Stephen McCrory<sup>6</sup>, Michael Zeher<sup>7</sup>, David Handelman<sup>7</sup>, Robert Griffin<sup>6</sup>, Sisir Karumanchi<sup>1</sup>, Christian Hubicki<sup>5</sup>, Brett Kennedy<sup>1</sup>, Jonathan Clark<sup>4</sup>, Jerry Pratt<sup>6</sup>, Dilip Patel<sup>3</sup> and Jason Pusey<sup>2</sup>

<sup>1</sup>Jet Propulsion Laboratory, California Institute of Technology

<sup>2</sup>U.S. Army Research Laboratory

<sup>3</sup>General Dynamics Land Systems

<sup>4</sup>STRIDe Lab, Florida State University

<sup>5</sup>Optimal Robotics Lab, Florida State University

<sup>6</sup>Institute for Human and Machine Cognition

<sup>7</sup>Applied Physics Laboratory, John Hopkin's University

**Abstract:** This paper presents the design, control, and initial performance from two iterations of human-scale (~75 kg) quadrupedal robots built under the U.S. Army Research Laboratory (ARL) Robotics Collaborative Technology Alliance (RCTA) LLAMA (Legged Locomotion and Movement Adaptation) project. These all-electric, quadruped robots are designed with custom quasi-direct-drive actuators powering 3-DOF, serial-parallel legs. To our knowledge, this is the first all-electric quadruped robot of this mass scale. The centralized energy management system uses a capacitor bank to supply burst loads and buffer regenerated energy. A hierarchical control scheme enables rapid motions (up to 1.8 m/s) over a variety of terrains. The onboard sensing suite enables deliberate, autonomous operation across rubble fields. In addition, we report on practical observations, lessons learned from field testing of two generations of the platform, and current drawbacks, such as low absolute payload (9 kg) and battery life (35 minutes). These lessons include strategies to address secondary effects at larger scales and parameters with the most impact to improve future designs.

**Keywords:** legged robots, control, mechanisms, terrestrial robotics

---

Received: 17 September 2020; revised: 9 May 2021; accepted: 11 May 2021; published: 22 March 2022.

**Correspondence:** Jay Jasper, Jet Propulsion Laboratory, California Institute of Technology,

Email: [jay.d.jasper@jpl.nasa.gov](mailto:jay.d.jasper@jpl.nasa.gov)

This is an open-access article distributed under the terms of the Creative Commons Attribution License, which permits unrestricted use, distribution, and reproduction in any medium, provided the original work is properly cited.

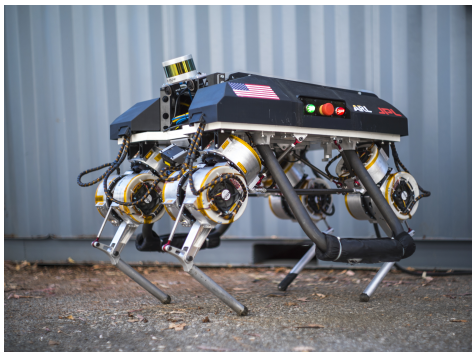
Copyright © 2022 Jasper, Kourchians, Gonzalez, Emanuel, Nicholson, McCutcheon, Austin, Kozlowski, Holmes, Hegeman, McCrory, Zeher, Handelman, Griffin, Karumanchi, Hubicki, Kennedy, Clark, Pratt, Patel and Pusey

## 1. Introduction

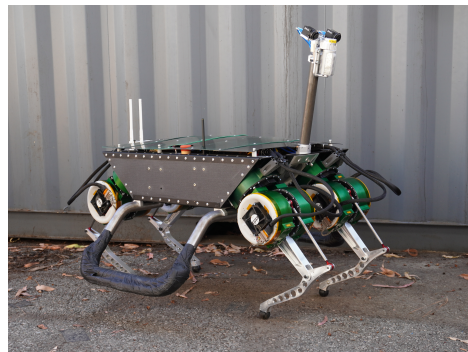
Current terrestrial robots have limited ability to quickly and efficiently navigate rugged terrain. This capability is needed for robots to be teammates to humans, from rescue workers to warfighters. This paper presents LLAMA, (Fig. 1a, b) an omni-directional, electrically-driven, human-scale ( $\sim 75$  kg), quadruped capable of rapid and autonomous operation in unstructured, natural environments. As a general trend, building the robot at a large scale should improve payload capacity and obstacle clearance for operating in rougher terrain (such as the rubble pile shown in Fig. 2). However, power requirements increase with size, mass, and locomotion speed. To address this dilemma, LLAMA was designed to be a research platform for large quadrupedal systems, to investigate their feasibility and the high power density technologies required.

Section 2 describes how LLAMA's design choices build upon recent developments in legged systems. Section 3 gives a summary of the robots' architecture developed over two platform generations and includes: (1) a custom quasi-direct-drive actuator designed to maximize torque and power density (2) an electrical energy management system to monitor and improve power efficiency and (3) a leg geometry designed for omnidirectional motion and motor load reduction.

Section 4 describes the reactive locomotion control software. Section 5 briefly summarizes a controller developed for deliberative locomotion. Section 6 presents initial results of the robots' capability including speed, robustness, and specific Cost of Transport (COT). Sections 7 and



(a) LLAMA 1.0 (2018)



(b) LLAMA 1.1 (2019)

**Figure 1.** The first iteration of the LLAMA platform has a mass of 73 kg and does not have a battery. The second iteration of the LLAMA platform has a mass of 70 kg total, including an 8 kg, 1.2 kWh custom lithium-ion battery pack. Both robots have 12 degrees of freedom and identical large-diameter, low-geared actuators that are 3 kg each. The actuators were revised between iterations.



**Figure 2.** Large robots are required for operations in regions with significant terrain roughness and complexity.

8 summarize the lessons learned from two generations of hardware development and provide concluding remarks.

## 2. Related work

### 2.1. Actuation

Actuators are a critical component of a legged robot; their mechanical capabilities establish locomotion characteristics, their electrical demands set the requirements for the robot’s electrical system, and they often represent a significant fraction of the total robot mass (Kenneally et al., 2016). Actuators and drive systems well-suited for dynamic legged locomotion have four characteristics: (i) high torque density<sup>1</sup>; the robot must be able to lift itself (ii) high speed; the foot must move quickly, especially while in the swing phase (iii) robustness to unexpected environmental interactions at significant velocity and (iv) able to control foot contact forces with closed-loop feedback controllers (Wensing et al., 2017).

Large, legged robots have predominately utilized hydraulic actuators, which have high robustness (characteristic iii) and can deliver both high force and high power (characteristics i and ii) when coupled with an appropriate pump. Notable examples include Boston Dynamics’s robots, the 360 kg LS3 (BostonDynamics, 2020a) and the 115 kg BigDog (Raibert et al., 2008). Istituto Italiano di Tecnologia (IIT) has developed a series of 80 kg quadrupeds called HyQ (Semini et al., 2015). Extremely large 6800 kg hydraulic quadrupeds have also been built (Doi et al., 2005). These robots are highly capable, but hydraulic actuation systems are loud and inefficient (Mattila and Virvalo, 2000).

A direct-drive actuator using a large electric motor excels at characteristics ii, iii, and iv but can only provide the required torque density (characteristic i) at small scales, as can be found in robots such as Ghost Minitaur (Kenneally et al., 2016). This limitation can be confirmed by examining a set of scaling laws. Assume the size scale of the robot is fixed due to mission requirements (big enough to handle a certain obstacle, but small enough to fit through a chosen opening). The performance of electric motors as measured by the motor constant ( $k_m : Nm/\sqrt{W}$ ) is *strongly* correlated to their gap radius (Seok et al., 2012), so the scale of the robot limits  $k_m$ . Assuming the biggest practical motor is already chosen,  $k_m$  will be treated as a constant. Thus, if the system mass doubles ( $m_R = 2$ ), the required actuator torque doubles, and the waste heat power ( $H$ ) due to torque production *quadruples*. The required actuator output power ( $P$ ) also increases linearly with system mass (consider gravitational potential  $mgh$  and kinetic energy  $1/2mv^2$ ). The implication for actuators is that input power increases proportional between  $m_R$  and  $m_R^2$  (depending upon torque production efficiency).

$$P_{act,ratio} = \frac{P_{act,new}}{P_{act,reference}} = \frac{m_R P + m_R^2 H}{P + H} \approx \begin{array}{l} \text{best case: } P_{act,ratio} \propto m_R^1 \\ \text{worst case: } P_{act,ratio} \propto m_R^2 \end{array} \quad (1)$$

The power challenges then propagate upstream to the battery pack, which not only has to supply the increased actuator load ( $P_{batt,load} \propto P_{act}$ ), but also dissipate heat due to internal resistance ( $P_{batt,heat} \propto R P_{batt,load}^2$  if the pack properties are held constant). The result is that required battery power can be very sensitive to mass increases ( $m_R^1$  to  $m_R^4$  depending upon design specifics). In particular, battery load is strongly affected by actuator waste heat ( $H$ ) as system mass increases, thus motivating the need to use actuator technologies with more efficient torque production.

$$\begin{aligned} P_{batt,ratio} &= \frac{P_{batt,load,new} + R P_{batt,load,new}^2}{P_{batt,load,ref} + R P_{batt,load,ref}^2} \\ &= \frac{(H^2 R) m_R^4 + (2HPR) m_R^3 + (H) m_R^2 + (P^2 R) m_R^2 + (P) m_R}{H^2 R + 2HPR + H + P^2 R + P} \end{aligned} \quad (2)$$

<sup>1</sup> Generalized force mass density. This paper will refer to torque and thus torque density exclusively; Nm / kg.

Most recent research has focused on all-electric legged robots of a smaller scale. Notable examples include Boston Dynamics's 32.5 kg Spot ([BostonDynamics, 2020b](#)), the quasi-direct-drive MIT Cheetah 3 ([Bledt et al., 2018](#)) and Mini Cheetah ([Katz, 2018](#)), and ANYmal (50 kg), which uses a serial-link limb architecture driven by series-elastic actuators to enable general purpose limb usage ([Hutter et al., 2016](#)). These robots are impressive, but in principle a larger-scale robot could have even more capabilities. LLAMA is designed to be an all-electric robot at a total-mass scale previously only occupied by hydraulic robots.

One approach to increase the torque density of electric actuators (characteristic *i*) without compromising robustness (characteristic *iii*) is to install a compliant element between the speed reducer's output and the actuator's output. A Series Elastic Actuator (SEA) measures the deflection of the compliant element to achieve force control (characteristic *iv*). ANYmal's actuators utilize this architecture, and are able to achieve a maximum torque of 80 Nm and maximum speed of 12 radians/second ([Hutter et al., 2016](#); [ANYbotics, 2021](#)). Challenges with this actuator architecture can include: decreased large-force bandwidth, increased control effort at high frequencies, and instability due to the decoupling of rotor and system inertias ([Robinson et al., 1999](#); [Pratt and Williamson, 1995](#); [Georgiev, 2019](#)). Variable stiffness SEAs have been designed to counter the limitations of fixed-stiffness SEAs, but they come at the cost of high volume and mass ([Jafari et al., 2011](#)).

A second approach to improve the torque density (characteristic *i*) while maintaining acceptable robustness (characteristic *iii*) is to use a quasi-direct-drive actuator. Actuators of this type use large gap radius (more effective at producing torque) motors and a gearbox with a minimum acceptable gear ratio, usually between 5:1 and 20:1. This approach is a direct trade-off; lower ratios provide poorer torque density, but increase gearbox efficiency and reduce reflected inertia thus increasing durability. The MIT Cheetah robots use this approach ([Seok et al., 2012](#); [Wensing et al., 2017](#); [Seok et al., 2013](#)), as does LLAMA.

The third architectural option is to include a clutch, so that in the event of a torque overload, control authority is temporarily lost in return for significant damage resistance (characteristic *iii*). Decoupling the problem in this manner changes the constraints on motor and gearbox selection, helping to enable high torque density (characteristic *i*) by using a higher-ratio gearbox. Boston Dynamics's Spot robot uses this architecture, with a clutch to provide overload protection and a harmonic gearbox (minimum commercially available ratio is 30:1) to increase torque density ([Potter et al., 2019](#); [Harmonic Drive, 2020](#)). However, without the spring deflection measurement of SEAs or clean current signal of (quasi) direct-drive actuators, accurate torque measurement (characteristic *iv*) for proprioceptive controllers becomes more challenging.

## 2.2. Energy management

Legged robots must be capable of handling regenerative energy loads imposed by reaction forces with the environment and antagonistic actuator configurations. This energy can either be dissipated as heat or buffered for reuse, increasing efficiency. There are two primary methods used for energy storage: mechanical storage using springs ([Folkertsma et al., 2012](#); [Hubicki et al., 2016](#)) or electrical storage using capacitors and/or batteries ([Seok et al., 2013](#); [Katz, 2018](#)). Storing energy using springs offers potentially higher efficiency (fewer conversions between different forms of energy), but comes with the penalty of a fixed spring constant at the legs, potentially limiting locomotion capabilities ([Nicholson et al., 2020](#)). Storing the energy electrically decreases efficiency, but allows for leg characteristics to be fully software-defined, enabling greater mobility. Storage of electrical energy can be implemented in a centralized or distributed topology ([Haueisen, 2011](#)).

The University of Tokyo developed a bipedal robot called HRP3La-JSK which uses a centralized 13.5 F electrical double-layer capacitor bank to source peak loads and sink regenerative energy ([Urata et al., 2010](#)). Capacitor banks typically have a lower Equivalent Series Resistance (ESR) than battery packs. The lower ESR allows for greater current loads and reduces waste heat. By allowing the capacitor bank to manage the high frequency current cycling (induced by robot's gait), overall stress on the battery pack is reduced, increasing safety and the battery's lifetime.

The power system must also protect the electrical components and payload from voltage transients induced by regenerative energy loads. Boston Dynamics’s Spot contains a clamping circuit designed to protect the battery voltage bus from exceeding the rated 72 V limit. Spot also implements a soft-start circuit at the payload interface to manage inrush currents when powering payloads with up to 300  $\mu\text{F}$  of bulk capacitance (BostonDynamics, 2020c).

### 2.3. Active compliance

Effective locomotion requires good control of both foot forces and foot position. It is not possible to realize force and position independently when a closed kinematic chain is formed by the terrain, body, and limbs. Active compliance addresses this trade-off at the software level. It has been an area of focus for legged systems since the early 1980’s (Klein and Briggs, 1980). Active compliance can be implemented either in an impedance or an admittance control architecture (Carignan and Cleary, 2000; Ott et al., 2015). Impedance control treats the robot as a torque-controlled system and computes deviations to torque set-points based on velocity and position error. In contrast, admittance treats the robot as a position-controlled system and relies on force errors to compute deviations to position set-points.

Impedance control is most common for quadrupeds (Seok et al., 2013; Park et al., 2014; Semini et al., 2015; Hutter et al., 2016; Hubicki et al., 2016). ANYmal (Hutter et al., 2016) uses an inner, torque-feedback loop with friction compensation and an outer PID controller for positions. This approach is well suited for ANYmal’s series elastic actuators, where the presence of a compliant element enables direct estimates of torque on the output side of the actuator. The proprioceptive control approach (Seok et al., 2013) relies on high *transparency* actuators that have low gearing. Foot forces can be estimated via applied actuator torques or currents after compensating for friction. The MIT Cheetah (Park et al., 2014) applies a simple PD controller to a desired foot force profile at the foot frame. The desired force is then transformed to actuator torque commands via inverse statics or inverse dynamics.

This work implements active compliance in the admittance control paradigm (in task space). This approach was chosen to avoid sensitivity to accurate mass, link inertia, and friction models needed to determine control inputs (torques) in the impedance paradigm. Each foot runs an independent controller that computes adjustments to desired foot position based on error between expected and estimated foot forces. The four foot-controllers were coupled via the reference foot forces generated at the robot level using a basic inverse statics model<sup>2</sup>. Inverse kinematics and proportional controllers transform desired foot forces to position commands sent to low level on-board position controllers within each actuator. Torque-dependent friction within the actuators was not modeled, even though the break-away current on the LLAMA actuators was non-negligible (0.7 A for version 1.0 and 0.5 A for 1.1). By using high-rate position control (kHz) via the EtherCAT protocol (Jansen and Buttner, 2004), actuator-to-actuator variations (due to low-cost manufacturing) can be ignored. This robustness reduces the dependence of the system on accurate mass models—a valued characteristic for field operations with unknown mass payloads.

## 3. System overview

LLAMA 1.0 (73kg) and 1.1 (70kg) are dynamic quadrupedal robots capable of omnidirectional motion and speeds upwards of 1.8 m/s. Each leg is driven by three identical electric actuators (Section 3.1) clustered on the proximal end of the leg to reduce inertial loads. These quasi-direct-drive actuators use a low gear ratio (5.25:1) to increase torque density while minimizing reflected inertia and providing a strong signal for current-based proprioceptive controllers.

<sup>2</sup>A wrench distribution problem was used to generate reference foot forces that rely only on mass, center of mass, and kinematics, which were easy to measure experimentally.

The robots' energy needs are met by a tether (both versions) or onboard lithium-ion battery pack (version 1.1 only). The research-focused actuator architecture limits payload (9 kg) and untethered operating time (approx. 35 minutes). An entire subsystem called the Energy Management Unit (EMU, Section 3.2) is responsible for monitoring and safely (dis)charging a large capacitor bank that handles the dynamic electrical loads. The robots' unique leg design is described in Section 3.3.

The robots' reactive locomotion controller (Section 4) is able to traverse terrain using only actuator feedback and the onboard Inertial Measurement Unit (IMU). Thus, the initially implemented forward-facing exteroceptive sensor suite is minimal: a stereo camera pair and 1-2 lidars. The reactive controller uses these sensors to avoid large obstacles (walls, trees, cars, etc.). A second, deliberative controller (based on (Griffin et al., 2017)) relies heavily on these sensors to carefully plan each footstep (e.g. stepping stones across a stream), enabling it to traverse rougher terrain than the reactive controller allows, but at a much slower pace. All computations for these controllers are completed by the robots' two onboard computers.

A review of project resources and the performance of each subsystem on version 1.0 led to a revision of the design. Changes were wide-ranging, and include improvements to the actuators, a new chassis design, and revised leg linkage geometry.

### 3.1. Large-diameter, low-g geared actuators

The leg-actuator system of a dynamic robot must balance torque density, impact absorption, and control bandwidth. On LLAMA, this objective is accomplished with a quasi-direct-drive architecture: a low-ratio gearbox and large diameter motor, with rigid kinematic chains between the rotors and foot. This architecture enables the use of current-based proprioception. To improve field serviceability and reduce cost, a single actuator design was used for all three joints of each leg (Fig. 3). Environmental protection was not a design priority, so these actuators only achieve IP10.

The performance envelope of the actuator is shown in Figure 4. Note the increased torque margin available for high performance maneuvers of LLAMA 1.1. Initial robot design (including actuator sizing) was performed using a simplified simulation in an iterative, manual process which is out of scope to discuss in this paper.

Brakes and motor controllers are not included in the actuators due to their perceived (in)direct mass cost. However, the mass of harnessing required between actuator and motor controller, and the challenges of mechanically and electrically protecting those signals, make distributed motor controllers a much more competitive option than originally assumed.

The single-stage, 5.25:1 planetary gearbox increases actuator torque density while remaining backdriveable (for current-based proprioception and regenerative efficiency) with only a moderate increase to actuator reflected inertia (for durability). The custom gears are module 2, AISI 9310 (chosen for having both high yield strength *and* high impact strength), normalized, then carburized to 0.3-0.7 mm case depth. A module 1 involute spline transmits torque from the rotor shaft to the sun gear while compensating for manufacturing errors in concentricity by introducing a small amount of backlash.

Testing of the LLAMA 1.0 robot revealed two deficiencies in the gearbox design which were rectified in the version 1.1 actuators. First, the coefficient of thermal expansion (CTE) mismatch between the steel ring gear and aluminum actuator housing caused the bonded interface to fail and slip at housing temperatures above 80°C. This problem was fixed by adding pins to that interface. Second, inertial impact loading broke the adhesive connection between the rotor shaft and spline. Data confirms that during impact events inertial loading dominates, and thus current limits cannot detect or protect any part of the actuator from these torque loads (Fig. 6). This problem was fixed by adding keys and changing to a different adhesive rated for higher temperatures. The durability, backlash, and efficiency (75%) of the version 1.0 actuator gearbox was deemed acceptable, so gear shape, size, material, and heat treatment remained identical.

To achieve the required torque, the low ratio gearbox is paired with a large frameless brushless motor (ThinGap LSI-160Y041A135H). This motor's high motor constant  $K_m = 0.605 Nm/\sqrt{W}$

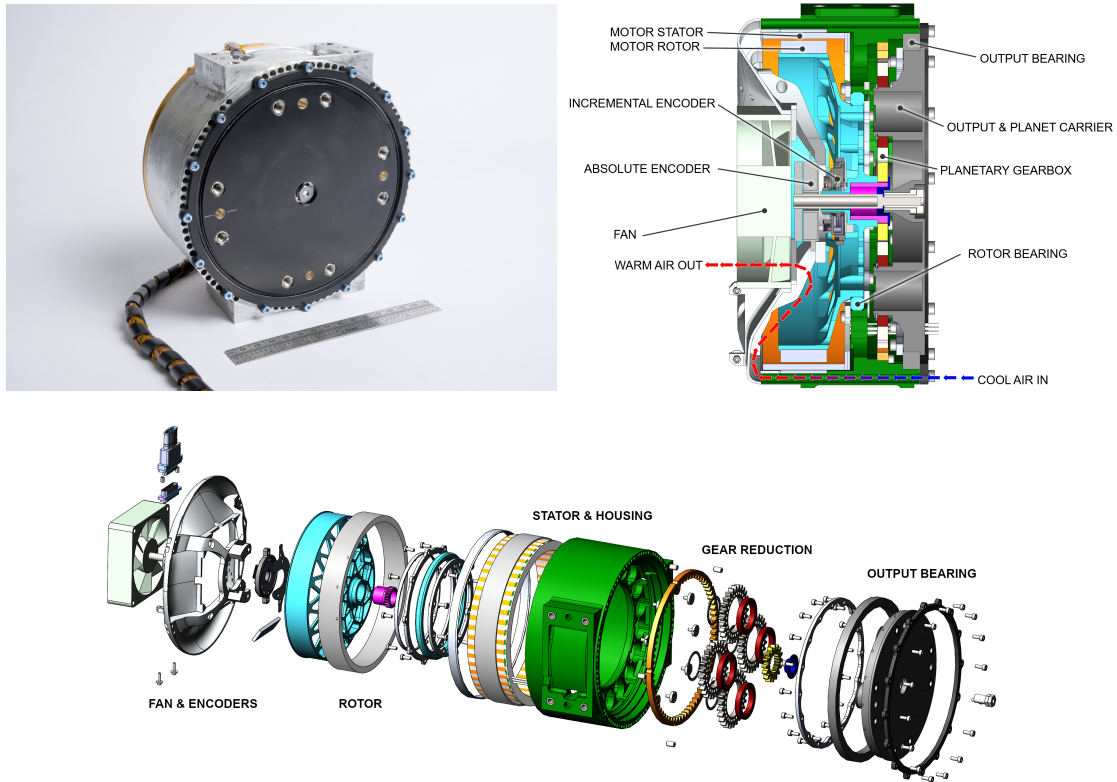


**Figure 3.** (a) The LLAMA 1.0 actuator has a mass of 3 kg and is shown with a 15 cm ruler for scale. The revised version 1.1 actuator is similar in mass and size. (b) LLAMA 1.1 actuator cross section. (c) LLAMA 1.1 actuator exploded view.

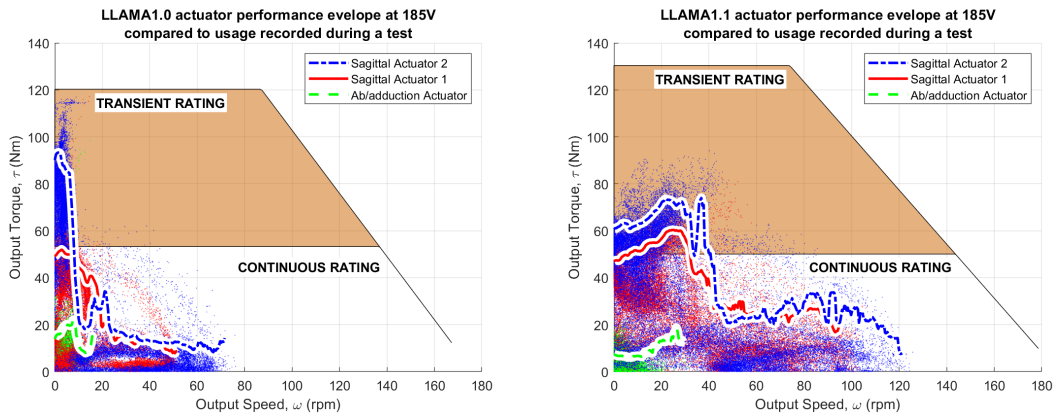


**Figure 4.** Plots comparing the actuator performance capability to usage, for a typical test of each robot. Lines represent the 90th percentile torque used at each speed. Performance differences between the robots are a combination of hardware changes (lower mass, altered leg kinematics), software improvements (variable gait frequency, altered foot placement), and operational state (commanding higher robot velocity).

reduces the waste heat for a given torque, while the ironless slotless toroidal winding potted directly into the housing minimizes thermal resistance out of the windings. The slotless architecture's zero cogging torque is a key feature for increasing the accuracy of current-based proprioception (Celera Motion, 2018).

A cross roller bearing (THK RA14008CUUCC0) reacts forces and cross moments on the actuator output. This bearing is rated for static cross moments of 1400 Nm (3.6x a static worst-case scenario), or static axial load of 43000 N.

### ***Thermal management***

Despite the design features intended to reduce the waste heat generated, under peak torque loading each motor still produces 1500 W of waste heat. The cost in mass and/or power to continuously shed this much heat from the robot is impractical. Instead, a low-mass, medium-capability cooling system was designed. Thus, the motors are intentionally transiently operated far outside the system's continuous cooling capability. This approach is compatible with legged robotics since, in general, shorter stance-phase duty cycle corresponds to higher loads, and vice versa. Active cooling is not a novel feature in legged robotics, but its use is less prevalent on small robots.

Each actuator incorporates an 80mm computer fan to cool the motor by drawing air through 68 holes in the housing, as shown in Figure 3(b). These small diameter holes extend the length of the housing and act as a heatsink, transferring heat from the housing to the air. While difficult to machine these features, implementing the heatsink with closed geometry (rather than a more traditional open-finned design) makes the heatsink an integral part of the actuator housing, a structural element that can support the robot's entire weight. The fan selection process compared hundreds of off-the-shelf fans to a simplified airflow-and-cooling model to select a fan with the appropriate balance between flow rate and static pressure capability while reducing mass, power consumption, and noise.

Four improvements were made to the thermal management system from LLAMA 1.0 to version 1.1. First, a thicker fan was selected (from 20 mm to 25 mm), calculated to provide a 19% improvement in cooling capability at the total cost of an additional 0.36 kg and 43W. Second, the airflow guide was modified to include a larger radius turning the airflow from axial to radial, thus reducing the pressure loss. Third, a second (redundant) temperature sensor was added to the housing exterior. Finally, the exterior of the actuator housing was anodized, increasing its emissivity and providing a small ( $< 10W$ ) boost to cooling capability. Figure 5 shows experimental data comparing the cooling performance of the two actuator generations, and confirming that the revised version 1.1 actuators have increased cooling capability.

Software changes were also implemented to reduce actuator heating. Figure 4 shows that by adjusting foot position (static offset applied before any of the controllers), the typical load is more evenly shared between the two sagittal actuators. This balancing not only reduces load (and heating) on the highest-loaded actuator, but since heat—and thus input energy—scales with torque squared, the balancing also reduces total robot energy consumption.

### ***Sensors for feedback and proprioception***

Each actuator contains an optical incremental encoder (Quantum Devices M-8192-0-A-A-N-B-A-L) on the rotor, initialized for commutation by a set of hall sensors, and zeroed with respect to the robot shape on startup by an inductive absolute encoder (Zettlex INC-8-37.063-171001-SSI1-RC372-5-S) attached directly to the actuator output. While the incremental encoder is the only sensor in active use for feedback and controls, the other rotation sensors are continuously monitored and an error is thrown if the incremental encoder readings are incompatible with the measurements from the other two sensors. The resolution (32,768 count/revolution) of the incremental encoder ensures the bandwidth of the velocity signal is acceptable even during low speed motions. This set of feedback sensors performed acceptably on version 1.0 and so was not changed for version 1.1.

Proprioception is accomplished by using actuator current alone as an estimate for actuator torque (torque at the gearbox output that interacts with the world). This approach was chosen to minimize



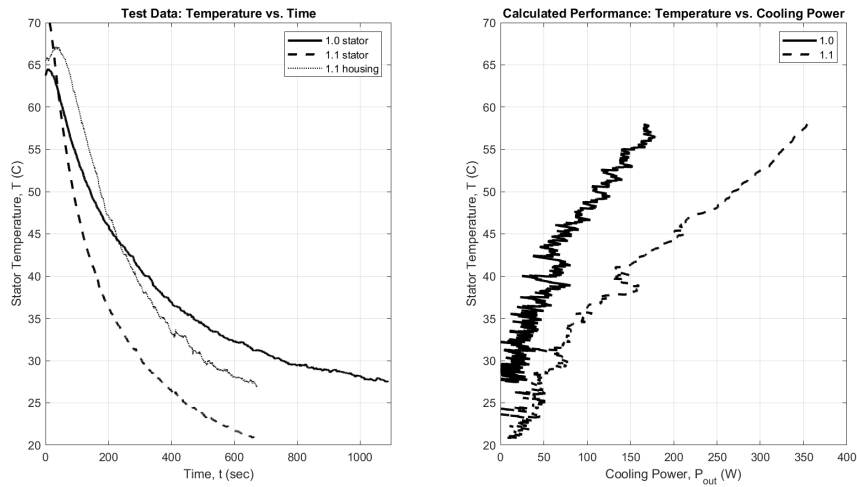


**Figure 5.** Validation of forced air cooling system by forcing current through motor until actuator temperature reached 70°C, then allowing to cool.

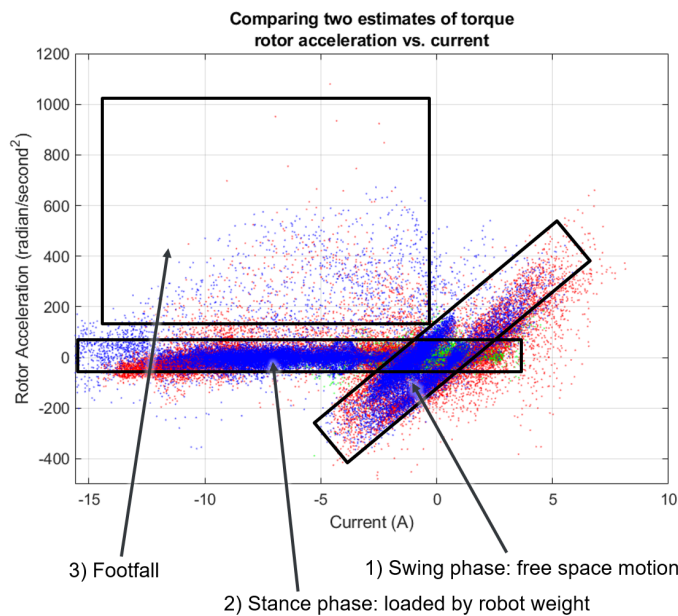


**Figure 6.** Evaluating the effectiveness of motor current as an estimate for actuator torque reveals challenges during impact events.

total system mass and simplify the system models used by the robot control software. This method is effective during both stance and swing phase as shown in Figure 6. During swing phase, a linear relationship is seen between rotor acceleration and current. Stance phase also exhibits a linear relationship between rotor acceleration and current, but the magnitude of rotor acceleration is much lower, since the actuator is now moving an inertia much greater than just its own. However, during impact events (footfalls), the measured actuator current *alone* is no longer a good signal for actuator torque. This behavior degrades the ability of software controllers to soften the limb (reduce the effective spring rate) and protect actuators against overload conditions during impact

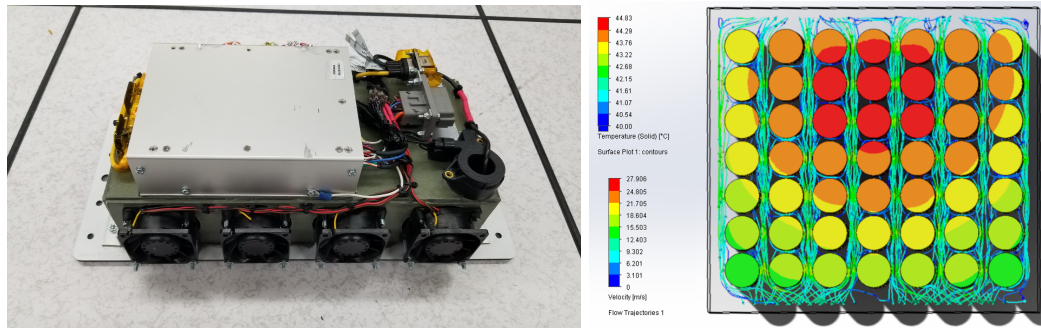


**Figure 7.** LLAMA 1.1 battery pack with integral cooling and battery management electronics. (best viewed in color)

events. Some version 1.0 actuator failures were attributed to this behavior, and so several mechanical interfaces were reinforced in the revised 1.1 actuators.

### 3.2. Electrical energy management

Individual, instantaneous actuator power requirements during legged locomotion can peak at values much higher than the system’s nominal net power requirement. On LLAMA, peak loads and energy buffering are handled by a large capacitor bank, while the net locomotion power is drawn from the onboard battery pack (or offboard power supplies). The nominal voltage of 185V on the high power bus was chosen to balance the greater efficiency and reduced cabling mass of high voltage systems with availability of low mass, off-the-shelf components.

The onboard energy source is a custom lithium-ion battery pack manufactured by CIE Solutions, shown in Figure 7. The battery cells (LG INR18650HG2) are arranged in a 46s2p configuration to provide 1.2 kW-hr at 115-193 V. Cell and pack health is monitored by an off-the-shelf Battery Management System (Orion BMS 2). For safety, cell surface temperature needs to remain below 45°C and isothermal (< 5°C between any two cells, < 1°C on an individual cell’s surface) but the high power draw generates significant heat within the battery pack: up to an average of 4.2 W/cell (386W total). This cooling requirement was met with forced air cooling. A finite element simulation combining fluid (CFD airflow) and thermal properties was used to select the fans. The fans are an integral part of the battery pack to enable offboard validation of the battery system. One unusual feature for safety is that a diode prevents any regenerated energy from recharging the battery.

An 18 mF (308 J) capacitor bank assists the battery in several ways. It (i) stores regenerated energy and buffers energy flow between antagonistic actuators, (ii) responds quickly to supply power for peak loading conditions, and (iii) reduces battery pack heating since peak loads are drawn from the capacitors which have a lower Equivalent Series Resistance (ESR) than the battery pack. Sizing the capacitors forces a trade between total stored onboard energy (battery mass) and burst energy available at very high power for short durations (capacitor mass). The capacitor bank on LLAMA was sized to handle the regenerated energy if the robot were dropped from 0.5 m. The resulting energy buffer is sufficient to keep the motor bus voltage fluctuation within 5 V during nominal trotting operations. This capacitance is approximately 15x what would be present on the motor bus if the motor controllers were used in their typical recommended off-the-shelf configuration, but still small compared to what is feasible with a bank of supercapacitors.

A specialized subsystem called the Energy Management Unit (EMU, Fig. 8) is responsible for controlling and monitoring voltage and current throughout the robot, as well as telemetry from the battery management system. The EMU provides this data to the onboard computer at 100 Hz. Two key states (capacitor and battery status) are used by the robot computer to ensure hardware safety during operations, but currently the majority of the EMU data is simply recorded for offline

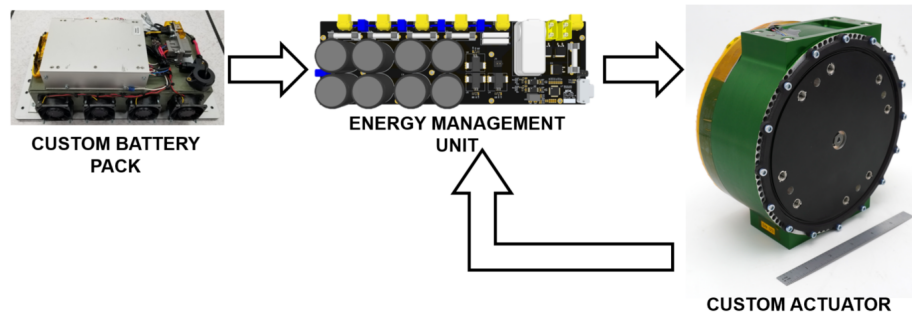


**Figure 8.** The Energy Management Unit (EMU) provides a centralized source for burst energy, buffers regenerated energy, and provides telemetry to study the flow of energy within the robot.

diagnostic and research analyses. The EMU is also responsible for (dis)charging the capacitor bank. For safety, the capacitor bank is drained any time the e-stop is activated or power is cut from the robot. The EMU will also cut power from the robot (except its own supervisory circuits) if a severe battery fault is detected. These safety precautions are critical due to the energy stored on a robot of this scale.

Several key improvements were made to the EMU as the robot was revised. First, the EMU expanded to include DC/DC converters and power distribution channels that were initially separate components, resulting in a significant reduction in mass and harnessing cost. Second, the mechanical main relay was replaced with a solid state relay. This change came at both a mass and efficiency cost, but was required after discovering that the soft start/stop circuit did not protect the main relay from welding during certain e-stop scenarios.

Keeping the computers alive for data recording even if the actuators brown out their power bus (temporary voltage drop causing loss of functionality or components to reset) was a major concern, and not solved satisfactorily. The initial design and testing of LLAMA 1.0 included a step-up converter from Elecdan Converter between the power source and motor bus. This converter would not only keep motor bus voltage up to maximize motor capability even as power source voltage dropped, but would limit the net power sent to the motor bus, thus always reserving power from the power source for computers. But because LLAMA 1.0 was overweight, the converter's 2 kW limit was problematic, so the converter was removed to save mass<sup>3</sup>. Additionally, testing at the time indicated the motor bus could drop as low as 150 V before affecting robot performance (see margin<sup>4</sup> in Fig. 4). Subsequently, the tether carried separate lines to power the motors and computers. The battery pack for LLAMA 1.1 was simply designed with large margins to provide enough power for most overload scenarios.

### 3.3. Legs

LLAMA's 3-DOF legs are driven by a cluster of identical actuators at the hip, in a series-parallel configuration. The proximal actuator is responsible for ab/adduction, while the distal two drive a parallel linkage providing motion in the leg's plane. The linkage architecture reduces the leg inertia experienced during rapid foot movements, but also limits foot workspace. A linkage was chosen instead of an alternative transmission (belt, chain, cable) for its load capacity. The use of identical motors for each joint requires the stiffness for each joint to be individually customized in software.

One unusual feature of LLAMA is the angle and configuration of the ab/adduction actuators. As shown in Figures 1 and 9, the distal pair of actuators are mounted as close as possible to the

<sup>3</sup> 0.75 kg not including heatsink and fans for 100 W of cooling

<sup>4</sup> Voltage available on the motor bus limits the maximum output speed. The output speed limit may decrease substantially before any of the recorded operating points would fall outside the limits.

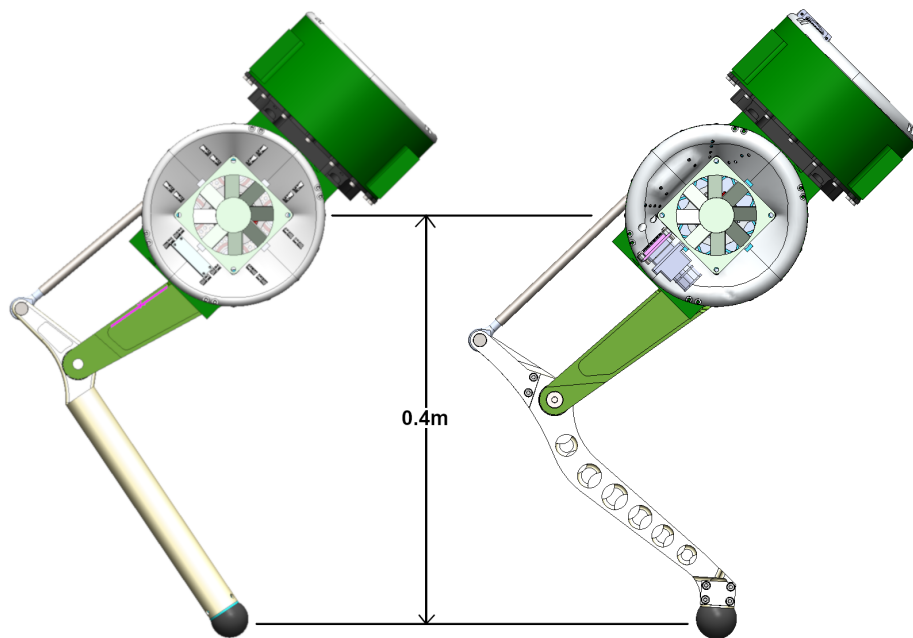


**Figure 9.** Minor changes to leg geometry from version 1.0 (left) to 1.1 (right) led to notable improvements in energy efficiency.

centerline of the ab/adduction actuator. This design has a variety of benefits, including reducing the structural loads, actuator effort, and inertia associated with ab/adduction moves. The ab/adduction actuators are pitched downward with respect to the chassis to reduce the loss of leg workspace due to self-collision (between the leg linkage and ab/adduction actuator).

However, this ab/adduction architecture has two key disadvantages. First, the singularity around the axis of the ab/adduction actuator encroaches on a commonly-used portion of the leg workspace. Second, the ab/adduction actuator spends much more time in the current deadband (nonzero current but zero output torque due to friction), decreasing accuracy of proprioception. These two disadvantages were recognized but addressing them is left to future work.

Two key improvements were made to the legs in LLAMA 1.1, resulting in the changes shown in Figure 9. First, the linkage kinematics were refined. Testing with the robot confirmed that in ‘real world’ situations, the robot only used a limited portion of its leg workspace. So optimization efforts successfully focused on expanding and improving performance in this ‘useable workspace’. Notably, the extension of the shin past the knee was lengthened, and the thigh and shin lengths were equalized, reducing the load on version 1.0’s higher-loaded actuator. The improvements can be seen in Figure 10. Second, the geometry of the shin was altered (keeping the revised underlying kinematics) to provide additional clearance to obstacles near the robot’s feet.

The feet consist of a layer of textured urethane overmolded onto a core. Refinements between the robot versions include additional padding (thicker urethane layer, change aluminum core to polycarbonate) and changes to reduce delamination (modified core geometry and overmolding surface preparation procedure). The spherical foot can be rotated to provide fresh contact surfaces as the urethane wears.

### 3.4. Body mass reduction

The chassis for LLAMA 1.0 was a mass-inefficient ‘breadboard’ (Fig. 11a), designed to provide a large and accessible mounting area for the electronics. The chassis for version 1.1 (Fig. 11b) was

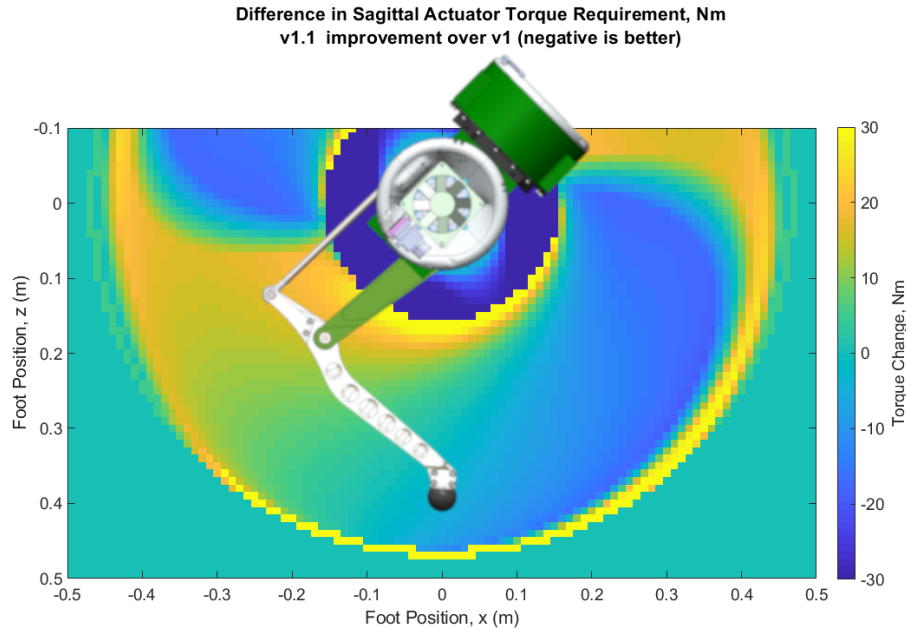
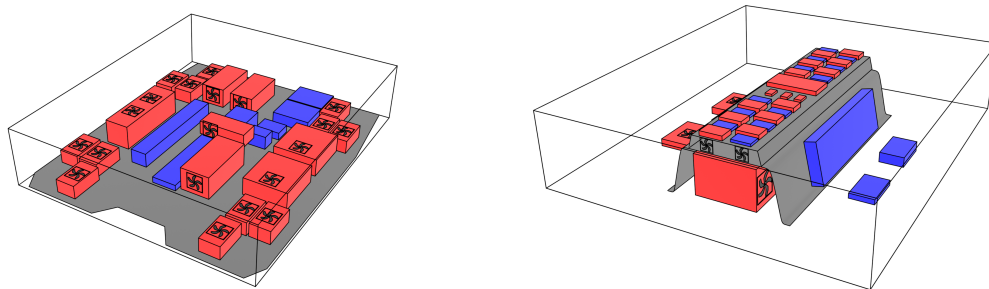


**Figure 10.** Worst case torque of in-plane (sagittal) actuators for a given leg geometry. Negative is better, indicating a reduced torque requirement. Note that the above analysis did not consider self collisions of leg links.



**(a)** LLAMA 1.0: breadboard-style, layout not optimized

**(b)** LLAMA 1.1: semi-monocoque structure with refined, carefully-placed electronics

**Figure 11.** Chassis electromechanical redesign yielded large mass savings and greatly reduced the quantity of fans required. Red color indicates components which required cooling.

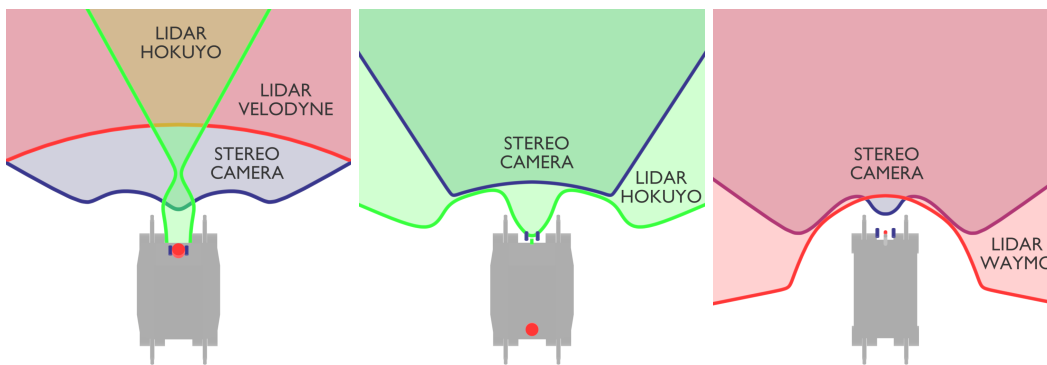
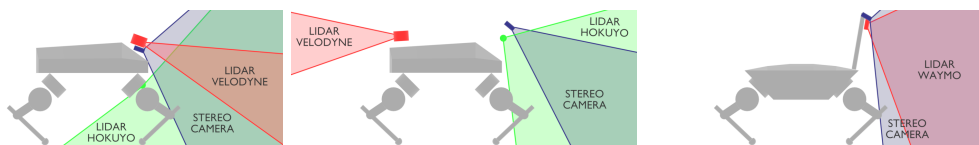
redesigned to have lower mass by using a semi-monocoque structure, combining multiple electrical subsystems onto the EMU PCBs (Section 3.2), and with careful layout to reduce wire harness lengths. The chassis was slightly reduced in size to allow the robot to be easily packed in a Pelican 0550 case for transport. The design changes were highly successful and resulted in 11 kg of mass reduction.

### 3.5. Exteroceptive sensing

The exteroceptive sensor suite consists of stereo camera pairs and lidars. The exact models and their placement were revised throughout the project. These revisions focused on improving sensing and field of view in the forward-facing 0.5 - 3 m range (near to the robot but not underneath it), and placing the sensors higher off the ground to enable more accurate measurement of nearby rough

**Table 1.** The exteroceptive sensor selection and placement was revised throughout the project.

Sensor	Model	Effective Field of View	1.0-Reactive	1.0-Deliberative	1.1-Reactive
Stereo camera	Point Grey (FLIR) FL3-U3-13E4C-C	120°	Height: medium Facing: front	–	Height: high Facing: front
Lidar	Velodyne Puck LITE	30°x 360°	Height: medium Facing: front	Height: medium Facing: rear	–
Lidar	Hokuyo UTM-30LX-EW on Dynamixel MX-106R servo	190°x 90°	Height: low Facing: front	Height: medium Facing: front	–
Stereo camera	Carnegie Robotics MultiSense S7	80°x 45°	–	Height: high Facing: front	–
Lidar	Waymo Laser Bear Honeycomb	95°x 200°	–	–	Height: high Facing: front

**Figure 12.** Comparison of ground visibility by exteroceptive sensors from the top. (best viewed in color)**Figure 13.** Comparison of the exteroceptive sensor fields of view from the side. (best viewed in color)

terrain. Table 1 enumerates the details, while Figures 12 and 13 visualize the changes from the top and side views respectively. The Waymo Honeycomb's field of view and point density allowed it to replace both the lidars used on LLAMA 1.0, aiding in mass reduction efforts.

#### 4. Baseline autonomy architecture

The baseline autonomy architecture was aimed at reactive locomotion and short range (< 100 m) point-to-point navigation with local maps. This architecture was chosen to be simple, easy to test and to be *loosely coupled with localization performance*.

The architecture consists of four nested control loops as shown in Figure 14. The outermost loop enables navigation and closes the loop with local exteroceptive sensing. The inner three loops use proprioceptive feedback to locomote over unknown terrain reactively. In this architecture, footsteps are not chosen deliberately according to terrain geometry.

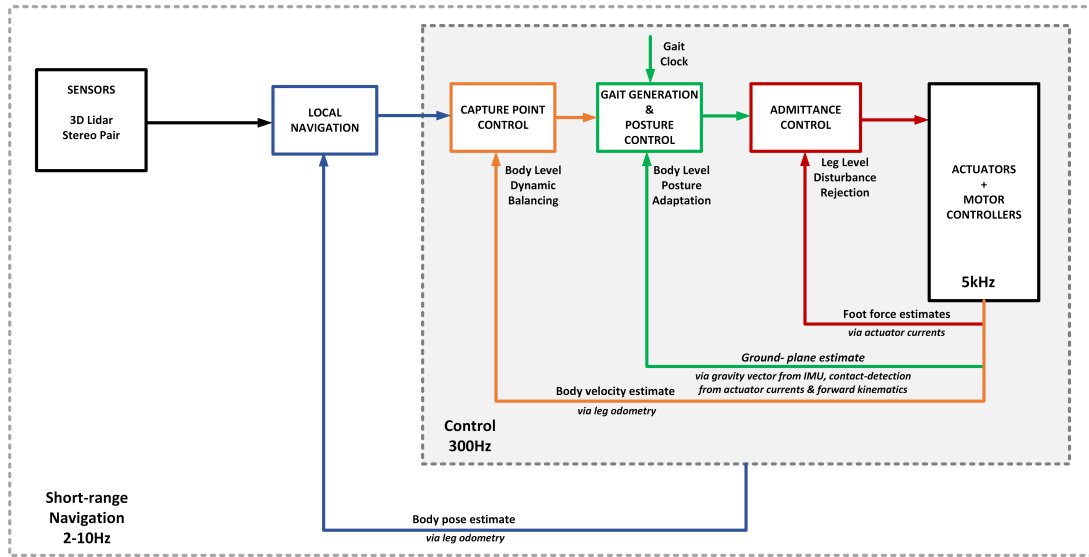


**Figure 14.** baseline autonomy architecture

The control loops consist of (i) a local navigation layer that runs at 2-10 Hz, (ii) a control layer that runs at 300 Hz consisting of body level velocity control (Capture Point), posture adaptation to slopes (Posture Control) and leg level disturbance rejection (Admittance Control), and (iii) actuator motor controllers running 5 kHz PD controllers (Motor Controller).

All calculations are performed in realtime by the robot’s two onboard computers. The computers are identical Intel NUCs (NUC7i7DNK1E: i7-8650U, 32GB RAM, 1TB SSD, integrated graphics) chosen for their x86 architecture to leverage previous software work. To reduce mass on LLAMA 1.1, the computers were removed from their cases and their wireless networking cards were replaced with M.2 SSDs.

#### 4.1. Notation

This section briefly summarizes the notation used in subsequent sections.

**Poses:**  $T_b^a$  is used to represent a homogeneous transformation from frame  $b$  to frame  $a$ .

**Twists:** The notation  $V_{a2b}^a$  represents twists with one superscript and two terms in the subscript<sup>5</sup>.

The superscript specifies the frame in which the twist is defined and subscript ( $a2b$ ) specifies that the twist is  $a$  to  $b$ .  $V_{a2b}^a$  is a spatial twist and it corresponds to frame  $b$  relative to frame  $a$  in the coordinates of frame  $a$ . Similarly,  $V_{a2b}^b$  is a body twist and it corresponds to frame  $b$  relative to frame  $a$  in the coordinates of frame  $b$ . The hat operator ( $\hat{V}_{a2b}^a$ ) is used to convert a  $6 \times 1$  vector into a  $4 \times 4$  matrix<sup>6</sup>.

**Velocities:** Notation similar to twists ( $v_{a2b}^a$ ) is used, but with smaller case  $v$  to represent the linear velocity of frame  $b$  relative to frame  $a$  in the coordinates of frame  $a$ .

**Foot Positions:**  $(x_i)$  is used to denote absolute position of the  $i$ th foot and  $\delta x_i$  is used to refer to relative corrections to the foot positions. A superscript (e.g.  $x_i^{robot}$ ) indicates the frame in

<sup>5</sup>This notation is consistent with that of (Murray et al., 1994) with the exception that the superscript is made explicit instead of  $s$  for spatial and  $b$  for body.

<sup>6</sup> $\hat{\xi} = \begin{bmatrix} \hat{\omega} & v \\ 0 & 0 \end{bmatrix}_{4 \times 4}; \hat{\omega} = \begin{bmatrix} 0 & -\omega_3 & \omega_2 \\ \omega_3 & 0 & -\omega_1 \\ -\omega_2 & \omega_1 & 0 \end{bmatrix}$

which the position is defined in (a robot frame). An additional subscript (e.g.  $x_{i,cmd}^{robot}$ ) is used to describe the purpose of  $i$ th foot position variable (e.g.  $cmd$  for commanded foot position).

**Foot forces:** ( $f_i$ ) is used to denote force at the  $i$ th foot and  $\delta f_i$  is used to refer to error between expected and observer foot force. As before superscript indicates reference frame.

## 4.2. Local navigation

Local navigation enables obstacle avoidance at the body level by re-planning quickly using the latest sensor information. The navigation layer runs at the frame rate of the slowest exteroceptive sensor and corresponds to the rate of re-planning with a D\* lite path planner (Koenig and Likhachev, 2002). On LLAMA 1.0, the slowest sensor was a scanning Hokuyo UTM-30LX-EW (Hokuyo, 2020) on a servo operated at 2 Hz, which limited re-planning to 2 Hz. On version 1.1, this sensor was replaced by a Waymo Honeycomb (Waymo, 2020) sensor that operates at 10 Hz.

Planning/re-planning is performed in robot frame with local traversability maps. Planning is not affected by localization performance. However, local navigation is loosely coupled with localization for the two reasons. First, motion compensation must be performed on scanning lidars based on local estimates of body velocity. Second, localization performance affects specificity of goals. Uncertainty on user-specified goals degrades with localization drift. This degradation will eventually render previously specified navigation goals obsolete. To manage this degradation, uncertainty on goal state is tracked, as opposed to robot state. Fast re-planning given local sensing scales to operation in dynamic scenes with moving obstacles such as people.

### *Leg odometry*

The leg odometry module generates real time estimates of body twist in the robot frame at 300 Hz. Given the body twist ( $V_{odo2robot}^{robot}$ ) the pose of the robot in an inertial frame (odometry frame) ( $T_{robot}^{odo}$ ) can be updated by a matrix exponentiation of the twist as shown below.

$$T_{robot}^{odo}(t) = T_{robot}^{odo}(t-1) * e^{(\hat{V}_{odo2robot}^{robot} dt)} \quad (3)$$

The body twist ( $V_{odo2robot}^{robot}$ ) defines the motion of a robot frame relative to an odometry ( $odo$ ) frame (in the coordinates of the robot frame). Even though odometry is imperfect and has drift, it is locally smooth for controls and sufficient for purposes of local navigation. It can be used to stitch together scanning lidar returns into a motion-compensated point cloud to form local maps that are refreshed at a rate of 2-10 Hz.

Body twist is estimated from observed joint velocities and angular rates from an IMU in a linear solver. Given current feet in contact, hip velocities relative to the foot in robot frame ( $v_{foot2hip}^{robot}$ ) can be determined from observed joint velocities  $\dot{\theta}_{leg}$  via forward kinematics. Foot-to-hip velocities and angular velocity measurement from the IMU are used as constraints to determine the body twist  $V_{odo2robot}^{robot}$  within a weighted least squares solver. Contact likelihood determines relative weighting between hip velocities. Leg contact forces estimated from actuators currents are used to determine a contact likelihood<sup>7</sup>. It is given by a logit model<sup>8</sup> similar to the one specified by (Camurri et al., 2017).

Given foot-to-hip velocities and angular velocity of the body, body twist is observable as long as two or more feet are in contact. In usage, this velocity-based estimator is simple and effective for trotting gaits where at least two feet are in contact at any given time. If less than two feet are in contact, then accelerations from the IMU will be needed.

### *Uncertainty tracking of navigation goals in the robot frame*

Goals specified in robot frame are modeled to have uncertainty associated with them using the formulation specified in (Barfoot and Furgale, 2014). Uncertainty on the body twist is modeled as

<sup>7</sup>  $f = J^T \tau = J^T k_{\tau} i$   
<sup>8</sup>  $\left( \frac{1}{1 + \exp(-\beta f - \beta_0)} \right)$



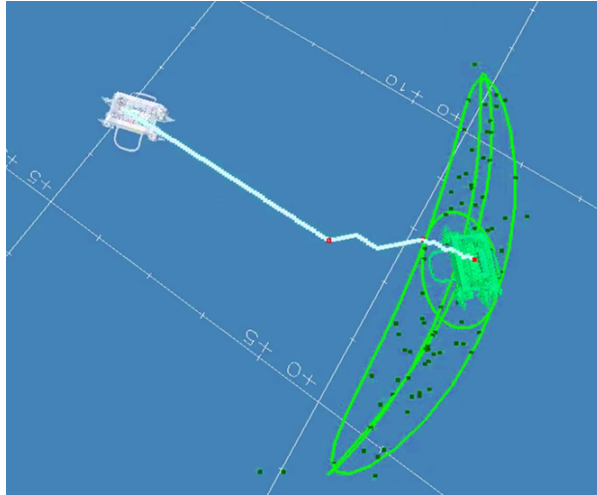


**Figure 15.** Tracking navigation goal uncertainty instead of robot state uncertainty. Given the latest sensor information, local navigation re-plans in robot frame every time-step to the operator specified goal. The uncertainty is used to either auto-update navigation goals or request updated goals from an operator. Green robot corresponds to the mean of the navigation goal and green lines are the projections of the great ellipses of twist ellipsoid to  $R2$ . (best viewed in color)

a Gaussian in six dimensions ( $V_{odo2robot}^{robot} \sim N(\mu_T, \Sigma_T)$ ). The mean and covariance of the body twist can be propagated and updated using the methodology described in (Barfoot and Furgale, 2014). This approach is a generalization of a Kalman filter to manifolds in  $SE(3)$ . Given the mean, the goal state is updated as follows.

$$T_{goal}^{robot}(t) = e^{(\hat{V}_{odo2robot}^{robot} dt)} * T_{goal}^{robot}(t-1) \quad (4)$$

The advantage of tracking uncertainty in twist space, is that it better represents the correlation between position and orientation. Such a framework is required as a small yaw uncertainty in robot state could result in a large variance of the position of a goal that is 100 m away. Figure 15 shows an example goal and its uncertainty represented in  $SE(3)$ . Uncertainty is shown via  $R2$  projections of the great ellipses of the twist ellipsoid defined in  $R6$ .

#### ***Fast re-planning with local traversability maps in the robot frame***

A dense representation of traversability is used as a cost map for path planning/re-planning in robot frame. A log odds update (Thrun, 2002)<sup>9</sup> framework similar to occupancy grids is used, but generalized to traversability derived from 3D point clouds. Similar to work presented in (Krüsi et al., 2017), traversability is assessed as a categorical event using surface normals derived for each point in the point cloud. If the surface normal in a gravity aligned frame is within a cone of feasibility, that point is marked traversable. Points above the robot head height are filtered out. Given a sparse, traversability-assessed point cloud, radial Gaussian process regression is used to derive a dense estimation of traversability and its uncertainty in a grid. Log odds update is then performed to update local traversability maps that are used as cost maps for path planning (see Figure 16). These maps are re-generated at 2-10 Hz. Each new map also triggers a re-plan.

<sup>9</sup> Given categorical events  $\{m, -m\}$  (i.e. yes/no, occupied/unoccupied, traversable/untraversable) and set of observations  $z_{1:t}$ , log of the odds ( $\frac{p(m|z_{1:t})}{p(-m|z_{1:t})}$ ) can be used to define a numerically efficient recursive update ( $l_t = l_{t-1} + \log\left(\frac{p(m|z_t)}{1-p(m|z_t)}\right) - \log\left(\frac{p(m)}{1-p(m)}\right)$ ). This is commonly used in occupancy grid mapping. In this work, it is adapted for traversability mapping

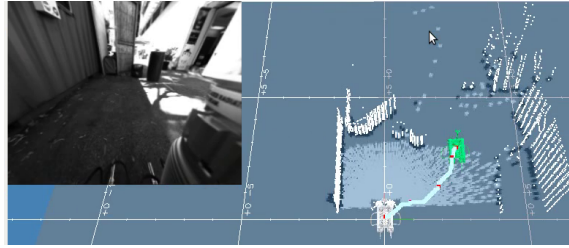


**Figure 16.** A screenshot from the operator station shows a single camera view overlaid on a 3D bird's eye view of the current (white) and desired (green) robot locations and a planned path (cyan). Raw point clouds from local sensing are shown in white. A local traversability map (gray scale image) is projected on the ground and is used as a cost map for path planning. In this map, dark areas are untraversable (probability 0), light areas are traversable (probability 1) and grey areas are unknown (probability 0.5). (best viewed in color)

### 4.3. Controls

The reactive controls strategy (shown within the grey box in Figure 14) consists of three nested loops that are coupled with feed-forward gait generation. They consist of (i) admittance control, (ii) posture control, and (iii) capture point control (Pratt et al., 2006). Admittance control is a force feedback loop which modifies foot position set-points based on a foot force error signal. This controller enables the robot to react to unexpected disturbances at the leg level. The middle loop (Posture control) is essential for managing workspace when traversing slopes. It uses a ground plane estimate to continuously manage posture, maintain static stability and prevent tip over (Fig. 17). The outermost loop is capture point control, which uses body velocity error to adjust gait parameters such as foot step direction and step size to dynamically counter disturbances at the whole body level.

Foot position is the common thread linking the nested control loops. Each layer adjusts desired foot position to meet its own goals, and in the end the control scheme treats the plant as a position controlled system. Inverse Kinematics turns foot position into joint angles and each joint is controlled at a high bandwidth (kHz)<sup>10</sup> via a position PD loop so as to compensate for friction and other higher order effects. Actuator-to-actuator manufacturing artifacts are handled via this high-bandwidth PD loop without requiring accurate friction models or system identification as would be needed with current control. Walking gaits are generated via feed-forward pattern generation within the control layer (after posture control and before admittance). Each of the layers are introduced and discussed in following sub-sections.

The sum of these layers (as shown below) produces  $x_{i,cmd}^{robot}$  which forms the final commanded foot position for the  $i$ th foot.

$$x_{i,cmd}^{robot} = x_{i,PC}^{robot} + \delta x_{i,gait}^{robot} + \delta x_{i,AC}^{robot} \quad (5)$$

$x_{i,PC}^{robot}$  originates from the posture control layer (PC),  $\delta x_{i,gait}^{robot}$  from feed forward gait generation and capture point control and  $\delta x_{i,AC}^{robot}$  from the admittance control (AC). The input to admittance control is a foot force error signal and the output is a modification of the foot position ( $\delta x_{i,AC}^{robot}$ ). The input to posture control is a ground plane estimate and the outputs are nominal foot positions which form an offset to feed-forward gait generation. Capture point control adjusts the parameters of feed-forward generation based on body level velocity feedback.

#### *Significance of Approach*

The main novelty of the architecture is the admittance control layer, which adjusts motor controller position set-points to track a desired force signal. This control loop is effectively a low-bandwidth

<sup>10</sup>The EtherCAT field-bus protocol is used to synchronize all joints at high rate.

force feedback loop around a high-bandwidth, soft position feedback loop. The desired force is a superposition of static equilibrium and dynamic stability correction terms (proportional controller on body orientation error). The effect is a dynamically changing system compliance, crucial in scenarios with uneven and unknown payload distributions on the robot.

Legged robots in rough terrain need to exhibit “soft” behaviors so unexpected interactions with the environment do not cause damage or loss of stability. Simply setting soft motor controller gains (80 Nm/radian; approx. 12 kN/m) was not a viable solution due to loss of control authority. Instead, “medium” stiffness motor controller gains (245 Nm/radian; approx. 38 kN/m) were used while relying on the admittance controller’s variable compliance capabilities to balance robustness and control authority. Signs of instability in the admittance layer started to appear at “high” stiffness (500 Nm/radian; approx. 77 kN/m).

Active compliance at the leg level can be achieved via admittance or impedance control frameworks. The former uses force measurements to adjust position set-points and later uses position feedback to adjust force or torque set-points. Both frameworks require forward models for inverse statics or inverse dynamics to either generate leg force set-points or to generate actuator torque commands. The admittance paradigm was chosen for LLAMA as this is less sensitive to the accuracy of system modeling, an important feature for handling unknown payloads. The high bandwidth position feedback at the actuator level also compensates for variations in actuators due to imperfect manufacturing.

### **Admittance Control**

At the lowest level, admittance is a force feedback loop which modifies foot position set-points based on a foot force error signal. The corrections are added to the feed-forward foot position generated by gait generation. As seen below,  $\delta f^{robot}$ , is the difference between the expected foot force,  $f_{des}^{robot}$ , and the current foot force,  $f_{cur}^R$ , where the superscript is used to show it is referenced in the robot frame.

$$\delta f^{robot} = f_{des}^{robot} - f_{cur}^{robot} \quad (6)$$

In particular,  $f_{des}^{robot}$  is defined as the forces required to support the body using the legs currently in contact with the ground. These forces are determined by a inverse statics model (via a wrench distribution problem) based on the desired posture generated by posture control. This term also utilizes the body orientation error to help stabilize the robot. Using the foot force error, the feedback term for determining the commanded foot position  $\delta x_{i,AC}^{robot}$  is defined as

$$\delta x_{i,AC}^{robot} = K \delta f^{robot} \quad (7)$$

where  $K$  is a admittance gain matrix ( $3 \times 3$ ) defined to reduce contact spikes and reject disturbances before and after contact occurs.

### **Posture Control**

Posture control (Fig. 17) takes as *input* a ground plane estimate in a gravity aligned inertial frame (Robot Centered Gravity Aligned, RCGA), orients the chassis parallel to this ground plane (increasing workspace), and shifts the center of mass above the center of pressure (increasing stability). The ground plane estimate is determined from the positions of feet in contact<sup>11</sup>. The *output* of posture control is new nominal foot positions  $x_{i,PC}^{robot_{new}}$ , which offset feed-forward gait generation to a continuously changing nominal stance posture that is a function of slope.

Using  $robot_{new}$  and  $robot_{cur}$  to represent new and current robot frames (the posture), the transformation matrices to an odometry frame (*odo*) from new and current robot frames is given

<sup>11</sup> Note that at least three feet are required to be in contact to estimate the ground plane. A short dwell/quadruple support phase ensured this requirement.

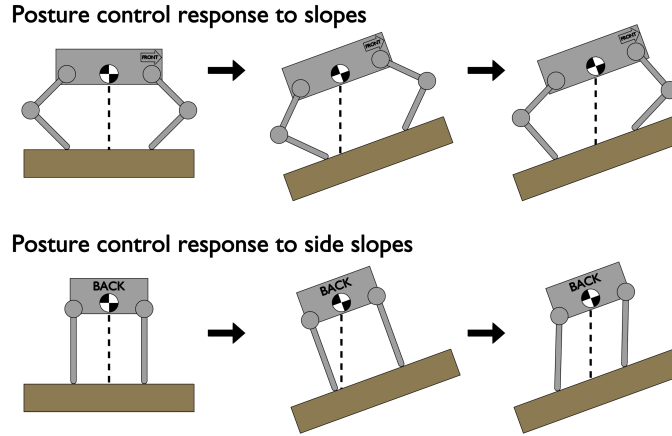


**Figure 17.** The posture controller alters foot position in response to a ground plane estimate to increase static stability and leg workspace.

as  $T_{robot_{new/cur}}^{odo}$ . The corrective transformation applied under posture control from current to new,  $T_{robot_{new}}^{robot_{cur}}$  may be expressed by an exponentiated twist form  $e^{\hat{\xi}^R dt}$  as shown below:

$$T_{robot_{new}}^{odo} = T_{robot_{cur}}^{odo} T_{robot_{new}}^{robot_{cur}} = T_{robot_{cur}}^{odo} e^{\hat{\xi}^{robot} dt} \quad (8)$$

Given  $\xi^R$ , the corrective twist on the body pose to align the body with the ground plane and shift the body's center of mass, new nominal foot positions are determined as follows:

$$x_{i,PC}^{robot_{new}} = (e^{\hat{\xi}^{robot} dt})^{-1} x_{i,PC}^{robot_{cur}} \quad (9)$$

where  $x_{i,nom}^{robot_{cur}}$  is the current foot command.

$$\xi^{robot} = \begin{bmatrix} \nu^{robot} \\ \omega^{robot} \end{bmatrix} = \begin{bmatrix} K_v f_{des} \\ K_\omega m_{des} \end{bmatrix} \quad (10)$$

Here,  $\nu^{robot}$  and  $\omega^{robot}$  are the translational and angular velocities,  $K_v$  and  $K_\omega$  are the velocity gains,  $m_{des}$  is a virtual body correction moment, and  $f_{des}$  is a virtual body correction force.  $f_{des}$  is defined using the error between the center of pressure of the robot, and the center of mass projected along gravity. The desired moment,  $m_{des}$ , is defined with a proportional controller on the orientation of the current nominal posture ( $q_{robot_{nom}}^{RCGA}$ ) with the desired posture given by the ground plane. The moment is generated by transforming the error quaternion ( $(q_{nom})^{-1} q_{des}$ ) to angle axis form.

### Capture Point Control and Gait Generation

At high speed, a legged robot cannot stop instantaneously. However, it can stop gracefully within a few steps. Capture point control enables the robot to achieve this requirement. Capture point control is based on a fictitious point on the ground (the Instantaneous Capture Point - ICP) where if a robot modeled as an inverted pendulum were to place and maintain its point foot it would come to a complete stop. Desired and actual ICP points are computed, and their relative error is used to adjust gait parameters such as foot step direction and step size to dynamically counter disturbances. Specifically, the capture point control law is

$$x = x_{des} + (1 + k_p)(\zeta - \zeta_d) \quad (11)$$

where  $x$  is the adjusted foot location,  $x_{des}$  is a feed-forward desired foot position based on the desired velocity of the robot,  $\zeta$  and  $\zeta_d$  are the current and desired Instantaneous Capture Points (ICP). The ICP error ( $\zeta - \zeta_d$ ) is used to compute foot step corrections and represents a form of

body level velocity feedback via regulating step size and direction.  $k_p$  is a control gain which must be positive to stabilize the robot. The Instantaneous Capture Point (ICP) control law used here was crafted using a similar method to those in (Krause et al., 2012; Griffin et al., 2017).

The feed-forward gait profile generates a ‘D’ profile which is defined by three parameters: a half step length, step lift and step direction. The origin of the ‘D’ (middle point of the straight line) is centered on foot position output of the posture control layer that represents the slope-adjusted stance. The gait generation is cyclical and is a function of a master clock phase with phase offsets for each foot. Foot phase offsets were fixed for a trotting gait which was default (Alexander, 1984). The half step size, step lift, and step direction are continuously modified by feed-forward reference velocity and feed-back capture point control based on Eq. 11. The output of feed-forward gait generation and feed-back ICP control is combined into a foot position adjustment ( $\delta x_{i,gait}$ ) for Equation 5. Note that capture point and gait generation are lumped together as capture point control adjust step parameters once per gait cycle and not all the time.

#### 4.4. Issues observed and Improvements from LLAMA 1.0 to 1.1

A guiding principle in the choice of baseline autonomy architecture was *ease of testing*. The central aim was to interleave development and testing in a layered manner starting from inner loops and moving towards the outer loop. This section briefly discusses some of the shortcomings of the architecture and notable design improvements that were made from LLAMA 1.0 to 1.1.

**Path chatter at fast re-planning rates:** Initial implementations of the local navigation layer suffered from path chatter in the D\* algorithm due to grid discontinuity. Grid-based planners such as D\* and A\* (Koenig and Likhachev, 2002) are known to generate sub-optimal paths as a function of grid discretization. The field D\* algorithm (Ferguson and Stentz, 2006) specifically address this shortcoming, but was not explored for this work. Since at each time-step, a new local map is used for planning, grid discontinuity can lead to excessive chatter, leading to instability. Chatter was reduced by planning in a hybrid frame that is robot centered but orientated to a global frame.

**Unreliable ground plane estimation in soft deformable terrain:** Posture control relied on a estimate of the ground plane in a gravity-aligned frame from proprioceptive sensing alone. At least three feet are required to be in contact to estimate the ground plane. A small dwell/quadruple support phase ensured this requirement. This behavior is an artificial constraint enforced to maintain stable ground plane estimation. LLAMA leg designs did not have contact sensors in the feet and so contact sensing relied on current feedback alone. High friction in actuators can make contact estimation via current feedback unreliable. This challenge was especially pronounced in soft deformable terrain. Ground plane estimation from exteroceptive sensing is worth considering. However, stable performance is non-trivial in real world conditions with dust, smoke, and deformable terrains.

**Limited leg workspace:** Compared to the state of the art, the current LLAMA leg designs have limited leg workspace. Workspace management for posture control became a significant time sink during testing. Premature workspace clamping lead to sub-optimal performance on slopes. A notable attempt was made in version 1.1 to optimize leg linkage design (Fig. 9 & 10), and enlarging the vertical workspace, improving the performance of posture control.

## 5. Extended autonomy architecture for deliberative navigation

One of the primary objectives for the LLAMA system was to successfully negotiate extremely complex terrain, such as that shown in Figure 2, which is characteristic of the challenging environments faced by the modern warfighter. In domains such as these, the number of available footholds for the robot are sparse, and their selection and ordering important. Consequently, traditional periodic-gait approaches are not applicable. To this end, a custom control system that models the environment



**Figure 18.** Left: Image of a rock field set up at Camp Lejeune. Right: Using the deliberative controller detailed in a companion paper (Griffin et al., 2021), the robot used lidar data to create a simplified model of the environment, then planned each footstep to traverse the obstacles using an A\* planner. The robot then successfully walked over the blocks, up the curb, and onto the inclined concrete slope on the other side.

then plans and executes specific footholds was designed. This system is described very briefly here, and more completely in a companion paper (Griffin et al., 2021).

The deliberative control system first models the environment by extracting planar regions from a lidar point cloud. Then footholds are planned using this environment model, given a desired body path or end goal from an operator or some high-level mission planner. These footholds are then provided to a custom, whole-body, momentum-control framework that regulates the robot's balance by tracking a desired Divergent Component of Motion (Takenaka et al., 2009). This momentum-control framework provides a compliant control architecture that gives the robot inherent robustness to environmental uncertainties. The whole-body controller then computes desired torques and joint accelerations for executing the specified motion while remaining balanced. These torque and joint acceleration setpoints are executed using a closed-loop impedance controller at the joint level. This approach was successfully demonstrated in a variety of experiments both at the IHMC Robotics Lab and at the RCTA Capstone Event at Camp Lejeune, shown in Figure 18.

## 6. Experimental Results

### 6.1. Locomotion capabilities

The omnidirectional, reactive, locomotion controller proved robust to a variety of conditions depicted in Figure 19. These include (i) surfaces of unknown stiffness (asphalt, floor pads, sand, soft dirt), (ii) loose objects that shift underfoot as they are walked on, (iii) slopes and side slopes, and (iv) external pushes. Videos of the robot may be seen at <https://tinyurl.com/llama-robot>.

The robot successfully completed an extensive, multi-day set of 70 field trials in 2018 at Camp Lejeune. The robot operated robustly on terrain that varied from concrete to soft sand, easily clearing small (<10 cm) obstacles, and carrying payloads up to 6 kg while traveling at speed (1.0 m/s) with minimal reduction in Cost of Transport. Omnidirectional locomotion capabilities enabled maneuvering through tight corners.

Despite these successes, both versions of the robot had room for improvement. The small leg workspace (particularly for v1.0) limited the robot's capability to adapt to steep slopes. Furthermore, sufficiently large (> 10 cm) unexpected obstacles caused the robot difficulty in remaining stable and on its feet.

#### *Admittance control performance*

The admittance controller is able to successfully maintain force goals (during stance phase) and position goals (during swing phase), as shown in Figure 20. During the stance phase, the force-tracking term dominates, successfully limiting the leg's peak ground reaction force to 75% of the robot's weight even though the the ground contact height varied greatly. During the swing phase,



**Figure 19.** Terrain successfully handled by the reactive locomotion controller

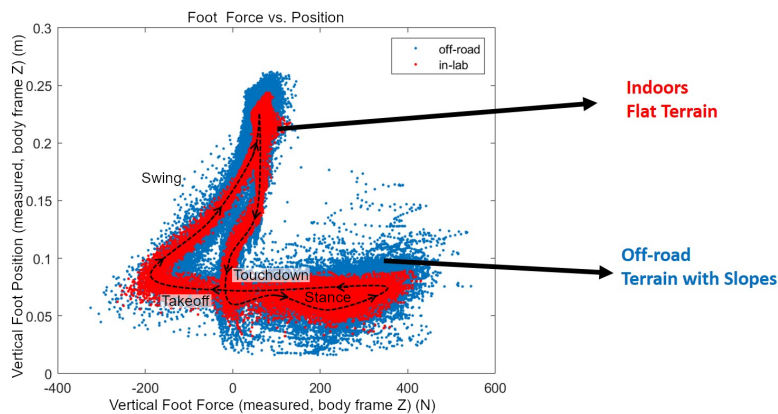


**Figure 20.** Plotting foot data in force-position space depicts the effectiveness of the admittance controller in achieving force goals during the stance phase, and position goals during the swing phase. The controller's gains are effective across a range of surfaces; a limit cycle is formed in position-force space. (best viewed in color)

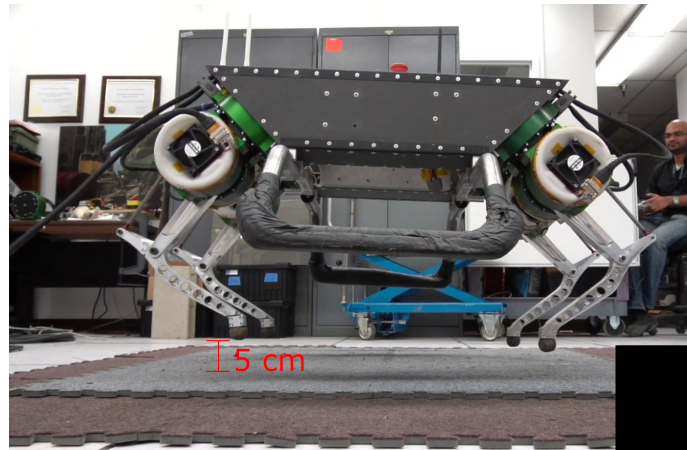
the position goals dominate, enabling the robot to lift its foot for clearance over obstacles. Controller performance is maintained on different surfaces without any alterations or changing of gains; a limit cycle is formed in position-force space.

### ***Jump attempt***

LLAMA was not designed to jump, but several attempts to do so clearly illustrated strengths and limitations of the design. Jumping is a test of actuation and power systems that can be used as a metric for robot agility (Haldane et al., 2016). The maximum attained jump height (Fig. 21) was only a few cm. Performance was limited due to the power system - all the energy in the capacitor bank was drained, the tethered power supply was unable to meet the burst power demands, and the motor bus browned out (temporary voltage drop causing loss of functionality or component resets). Due to the independent low voltage power supply, all the robot's computing, motor controllers, and sensors remained fully powered throughout the test and the robot landed safely. This test

**Table 2.** Comparison of the cost of transport for different robots.

Robot	Cost of Transport ( $P/mgv$ )	Note
LLAMA	5-30	Velocity-dependent, 95 <sup>th</sup> percentile
MIT Cheetah Cub	6 - 12	Velocity-dependent (Spröwitz et al., 2013)
MIT Cheetah 1	0.51	Best performance (Seok et al., 2013)
MIT Cheetah 2	1 - 4	Velocity-dependent, +1 standard deviation (Park et al., 2017)
MIT Cheetah 3	0.45 - 1	Velocity-dependent, 1 second averages, trotting gait, (Bledt et al., 2018)
ANYmal	1.2	best performance (Hutter et al., 2016)

**Figure 21.** Insufficient availability of burst energy limited LLAMA's jumping capabilities.

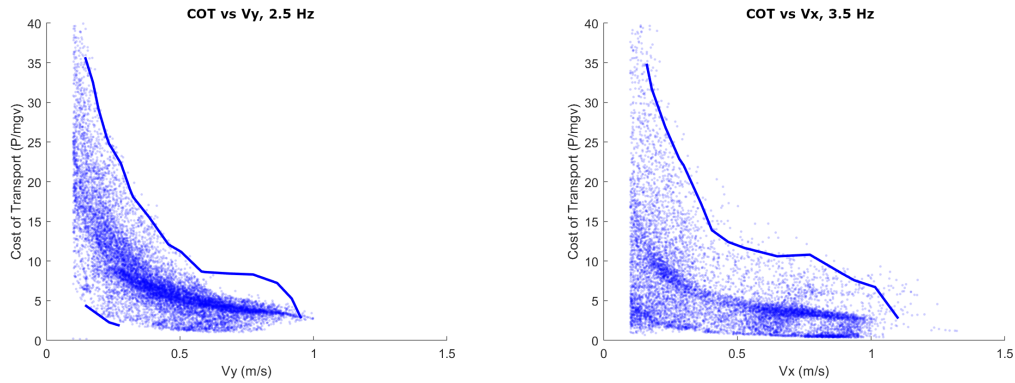
underscores the need for a power system architecture capable of handling scenarios in which burst locomotion loads threaten to brown out the entire robot.

## 6.2. Efficiency improvements from robot revision

Cost of Transport (COT) versus velocity curves were measured for both revisions of the platform under varying conditions. COT quantifies the energy consumption of locomotion (lower is better), and is an important metric for assessing how practical a system is in the field, where it must be energy-independent. Table 2 summarizes the COT performance of LLAMA in comparison to other quadrupedal robots. In all cases, cost of transport is lowest at the robot's maximum speed, and steeply increases as speed decreases. This trend is consistent even in a much smaller robot with a different (compliant) leg architecture (Spröwitz et al., 2013). One key implication of this trend is that any robot speed limits imposed by autonomy and planning software will result in a higher cost of transport and thus decreased robot range compared to its range under teleoperated control.

Figure 22 illustrates the process by which the cost of transport curves reported here were constructed. Raw test data provided many points of instantaneous robot speed and power consumption. The cost of transport at a given speed is the 95<sup>th</sup> percentile cost of transport for data recorded near that speed. This analysis technique captures the variability inherent in real-world applications outside of a pristine lab environment. The omnidirectional capabilities of the robot were approximated by separate analyses of the forwards and sideways velocity components. The cost of transport experiments did not push the robots to their maximum velocity and so the data presented here does not quantify the increased velocity capability of version 1.1.

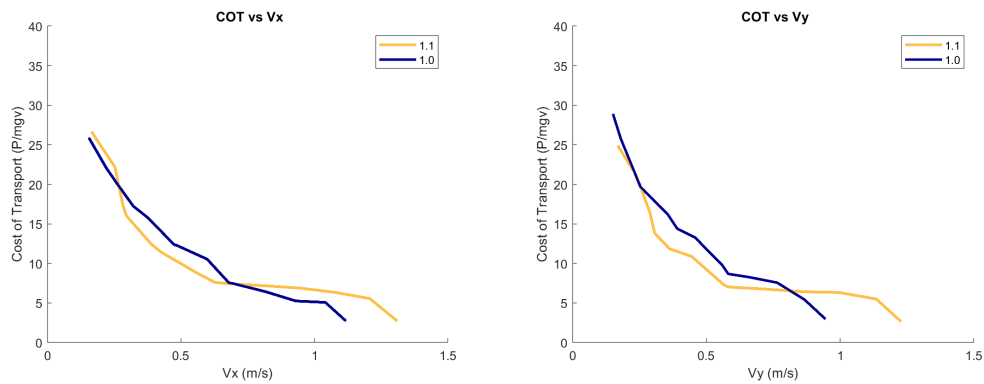




(a) Cost of transport for LLAMA 1.0 at 2.5 Hz stride frequency when moving sideways

(b) Cost of transport for LLAMA 1.1 at 3.5 Hz stride frequency when moving forwards

**Figure 22.** Representative scatter plots of cost of transport ( $P/mgV$ ) performance vs. velocity. The solid lines are the 95<sup>th</sup> percentile cost of transport at a given speed. Since data on a specific speed is sparse, the 95<sup>th</sup> percentile statistics are computed for small speed ranges (0.1 m/s). The 95<sup>th</sup> percentile curves are used in subsequent plots for comparison.



(a) Cost of transport vs. forward velocity

(b) Cost of transport vs. side velocity

**Figure 23.** LLAMA 1.0 (blue) vs 1.1 (orange): Cost of transport ( $P/mgV$ ) performance vs. velocity (m/s) (forwards and sideways) at 2.5 Hz stride frequency.

Cost of transport performance of the two versions is compared in Figure 23. For both cases, data was taken from an example run that included both fore-aft and lateral trotting. The revisions to LLAMA 1.1 resulted in a small reduction of the cost of transport, and an increase in the maximum attainable speed.

### 6.3. Actuator power flow and regeneration

Examining the flow of mechanical power in and out of a single actuator (Fig. 24) yields insights into the robot's performance and potential improvements. The Energy Management Unit (EMU) is frequently active, absorbing regenerated energy. Regenerated energy is particularly notable during the quadruple-support dwell periods at takeoff and landing, where the robot pauses momentarily to get a better estimate of ground plane orientation. Significant negative work is done by both sagittal plane actuators in the middle of the stance phase, hinting that the controller may be adding too much energy to the system in the early part of the stance phase. Finding a clear cause for

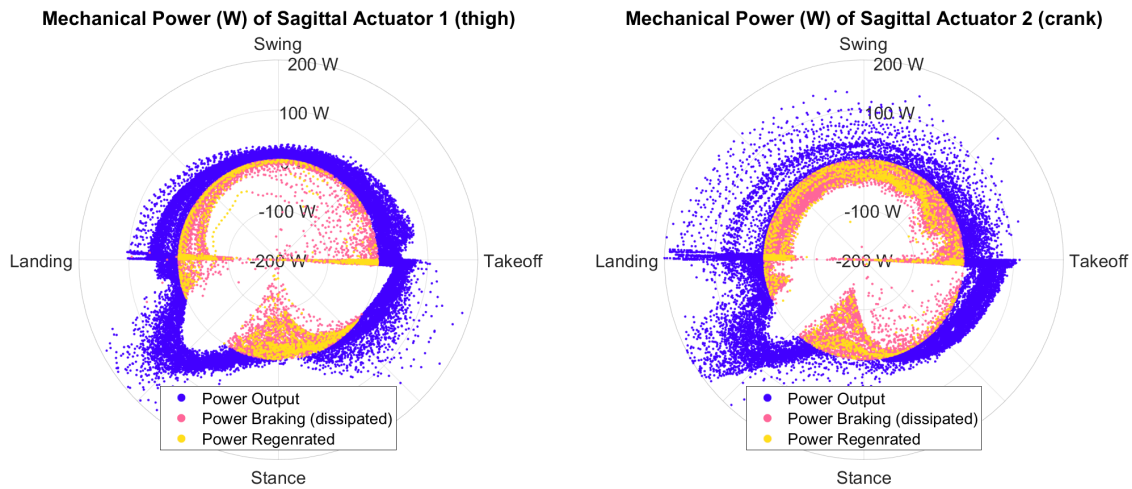


**Figure 24.** Instantaneous power states of two sagittal actuators over time versus the open-loop, gait-cycle clock. Positive values indicate the robot is adding to its kinetic or potential energy. Negative loads are distinguished between those resulting in some electrical-energy recovery and those fully dissipating as heat. Note the gait-cycle clock does not advance linearly with time, but has a rate adjusted as a function of robot speed and pauses at landing/takeoff to attain quadruple support.

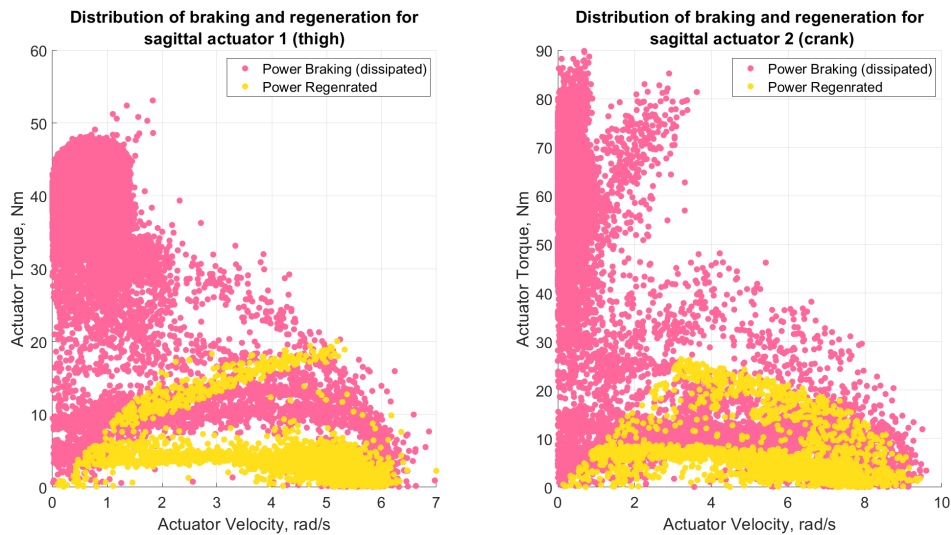


**Figure 25.** Energy regeneration is most effective at low torque, where the amount of negative work lost due to heat is minimized.

this behavior is a topic for future research. A second opportunity for future improvement is in the swing phase, where stiff position control has caused the power state to chatter, at non-negligible amplitudes, between power output and regeneration/braking, thus wasting energy as heat in the process. Also notable is that the magnitude of negative mechanical power does not correspond to whether or not a portion of that power is regenerated (yellow dots in Fig. 24) instead of being fully dissipated as heat within the actuator. Instead, efficient regeneration correlates with with low *torque* states that convert less of the negative energy to heat, shown in Figure 25.

## 7. Lessons learned

The following are some of the lessons learned in building a human-scale, all-electric quadruped.

### Large electric quadrupeds

*Large, all-electric quadruped platforms are feasible at human scales.* This work examined the feasibility of 75kg-class dynamic quadrupeds. While the platforms described here are unlikely to be viable for any real-world application, they are a functional point-design that can be used for scaling future solutions. In particular, since motor size is already maximized, gear ratio is the most influential design parameter. Increasing the gear ratio while maintaining the output torque capability can provide reductions in actuator mass and substantial reductions in waste-heat cost due to Joule heating. These parameter sensitivities are a function of the parameter values; LLAMA has high-mass motors and a low-reduction-ratio gearbox, so a small percentage decrease in motor performance can buy a large percentage increase in gear ratio (Wensing et al., 2017).

### Scaling up

*Nonlinear scaling laws turn secondary effects into significant challenges at large scales.* Due to nonlinear scaling, secondary effects (heat and EMI) become significant in high power robotics and cannot be ignored. These effects cascade far upstream. For example, high thermal losses in actuator and motor controller require additional cooling fans, increasing load on DC/DC converters, which then require augmenting their own cooling solutions. While the robot's actuators have enough torque and mechanical power to be capable of jumping, this action also causes a 12 kW burst waste heat load. The power system—designed for a trotting load case—was unable to meet this combined burst demand and the motor bus browned out.

### Operational speed

*Autonomy may constrain speed below raw platform capability.* Under teleoperated control in favorable conditions, LLAMA 1.1 achieved forward speeds of  $> 1.5$  m/s while, under autonomous control, speed was limited to 0.8 m/s. This operational speed was enabled by a 10 Hz local replanning rate—fast enough to operate among moving obstacles without specialized tracking routines—and the system's tolerance for imperfect perception data. Autonomous operations at 1.2 m/s can be achieved by augmenting the exteroceptive sensor suite to provide a sufficiently dense local map at a range of 20 m. Since the cost of transport decreases with speed, slowdowns from autonomy software also limit the robot's effective range.

### Reliability

*High-reliability practices are required, not optional.* Robot reliability excelled where careful design and disciplined handling were utilized. LLAMA 1.0 completed a 4-day, 70-test set of field trials in 2018 at Camp Lejeune with zero hardware issues. The LLAMA 1.1 actuators had zero problems during the entire 19-day shakeout testing phase. In particular, the use of military-grade connectors provided version 1.1 substantial reliability improvements over version 1.0. Reliability doesn't end with design, but must be continuously enforced in assembly and maintenance of the robot. The team's standard procedures included cleaning of parts before assembly, threadlocker, and torque wrenches. Electronic Printed Circuit Boards (PCBs) were populated using an incremental, iterative, assemble/test process to catch flaws early. Sources of potential issues—in particular electrical noise (EMI) and software timing jitter—were carefully investigated and resolved.

## Ground sensing

*Ground sensing is a critical challenge that has a huge influence on robot performance.* Contact conditions govern discrete changes in the system being controlled. Calculating an estimate of the ground's orientation underneath the robot enables the robot to operate on slopes. Actuator-current-based contact sensing at this large scale proved challenging and the required filtering for robustness lacked flexibility and introduced delays in contact detection. Pre-contact ground estimates could provide the robot more control over foot contact state and thus reduce periods of underactuation. Event-based control architectures may also improve the robustness of ground sensing.

## 8. Conclusions

The LLAMA robots were developed for the Army Research Laboratory (ARL) under the Robotics Collaborative Technology Alliance (RCTA) to investigate high power, human scale quadrupeds and push the boundary of what is feasible with electric actuators. Nonlinear scaling laws amplify electromechanical challenges at this large scale, from structural loading to thermal control to electromagnetic interference.





These robots have demonstrated locomotion through a range of surface conditions while relying solely on onboard power and computing. Custom actuators and power electronics were developed to enable a quasi-direct-drive legged platform at 75 kg scales. A central energy management system allows safely sharing regenerated energy among limbs. The hierarchical control structure divides system goals into subproblems that can be addressed by straightforward controllers in a frame that best suits each subproblem and is robust to inaccurate mass models of the robot. Planning is computed in local space to minimize the impact of localization error and to enable rapid replanning in scenes with moving elements. Lessons from the first version resulted in 11 kg (15%) mass reduction in a second, more capable version.

Large, all-electric quadrupeds are feasible, but energy efficiency remains a barrier to making such systems viable in field applications. The quasi-direct-drive architecture, currently popular at smaller (5-25 kg) scales, is impractical at large (75 kg) scales. Further development of large, dynamic robots requires the utilization of higher-ratio (than LLAMA's 5.25:1) gearboxes to increase the actuator torque density and reduce waste heat generation. This requirement motivates further investigation into the gear-ratio limits of quasi-direct-drive architectures and improved technologies for overload protection, contact detection, and load measurement. Advances in autonomy software are also required, both to handle more rugged terrain and to allow the robot to operate autonomously at higher speeds, thus reducing the effective cost of transport.

### 8.1. Acknowledgments

The work described in this publication was carried out at the Jet Propulsion Laboratory, California Institute of Technology, in collaboration with Autonomous Systems Division, U.S. Army Research Laboratory; Information Sciences Division, U.S. Army Research Laboratory; Autonomous Systems, General Dynamics Land Systems; Florida Institute for Human and Machine Cognition (IHMC); STRIDe Lab, Florida State University; Optimal Robotics Lab, Florida State University; Applied Physics Laboratory (APL), John Hopkin's University under the Robotics Collaborative Technology Alliance (RCTA) agreement #W911NF-10-2-0016.

### ORCID

Jay Jasper  <https://orcid.org/0000-0002-1216-936X>  
 Mark Gonzalez  <https://orcid.org/0000-0002-7531-5774>  
 John Nicholson  <https://orcid.org/0000-0002-4798-7856>  
 Sisir Karumanchi  <https://orcid.org/0000-0002-0685-4125>

Christian Hubicki  <https://orcid.org/0000-0002-2092-3772>

Jerry Pratt  <https://orcid.org/0000-0001-8414-5220>

## References

- Alexander, R. M. (1984). The gaits of bipedal and quadrupedal animals. *The International Journal of Robotics Research*, 3(2):49–59.
- ANYbotics (2021). ANYmal C Legged Robot. <https://www.anybotics.com/anymal-legged-robot/>. Accessed: 2021-01-29.
- Barfoot, T. D. and Furgale, P. T. (2014). Associating uncertainty with three-dimensional poses for use in estimation problems. *IEEE Transactions on Robotics*, 30(3):679–693. doi: 10.1109/TRO.2014.2298059.
- Bledt, G., Powell, M. J., Katz, B., Di Carlo, J., Wensing, P. M., and Kim, S. (2018). Mit cheetah 3: Design and control of a robust, dynamic quadruped robot. In *2018 IEEE/RSJ International Conference on Intelligent Robots and Systems (IROS)*, pages 2245–2252. IEEE.
- BostonDynamics (2020a). Boston Dynamics Legacy Robots: Legged Squad Support System (LS3). <https://www.bostondynamics.com/legacy>. Accessed: 2020-03-13.
- BostonDynamics (2020b). Spot. <https://www.bostondynamics.com/spot>. Accessed: 2020-03-13.
- BostonDynamics (2020c). Spot Payload Hardware Reference Manual RC1. <https://www.bostondynamics.com/sites/default/files/inline-files/spot-payload-hardware-reference-rc1.pdf>. Accessed: 2020-07-31.
- Camurri, M., Fallon, M., Bazeille, S., Radulescu, A., Barasuol, V., Caldwell, D. G., and Semini, C. (2017). Probabilistic contact estimation and impact detection for state estimation of quadruped robots. *IEEE Robotics and Automation Letters*, 2(2):1023–1030. doi: 10.1109/LRA.2017.2652491.
- Carignan, C. R. and Cleary, K. R. (2000). Closed-loop force control for haptic simulation of virtual environments.
- Celera Motion (2018). Comparison of slotless and slotted motors. <https://www.celeramotion.com/applimotion/support/technical-papers/slotless-vs-slotted-motors/>. Accessed: 2018-06-27.
- Doi, T., Hodoshima, R., Hirose, S., Fukuda, Y., Okamoto, T., and Mori, J. (2005). Development of a quadruped walking robot to work on steep slopes, TITAN XI (walking motion with compensation for compliance). In *2005 IEEE/RSJ International Conference on Intelligent Robots and Systems*, pages 2067–2072. IEEE.
- Ferguson, D. and Stentz, A. (2006). Using interpolation to improve path planning: The Field D\* algorithm. *Journal of Field Robotics*, 23(2):79–101. doi: 10.1002/rob.20109.
- Folkertsma, G. A., Kim, S., and Stramigioli, S. (2012). Parallel stiffness in a bounding quadruped with flexible spine. In *2012 IEEE/RSJ International Conference on Intelligent Robots and Systems*, pages 2210–2215. IEEE.
- Georgiev, N.-Z. (2019). *Towards High Performance Robotic Actuation*. PhD thesis, Caltech.
- Griffin, R., McCrory, S., Bertrand, S., Calvert, D., Lee, I., Stephen, D., Neuhaus, P., Jasper, J., Karumanchi, S., Kourchians, A., Holmes, E., Hegeman, R., Pusey, J., and Pratt, J. (in print, 2021). Compliant quadrupedal walking over complex terrain. *Field Robotics*.
- Griffin, R. J., Wiedebach, G., Bertrand, S., Leonessa, A., and Pratt, J. (2017). Walking stabilization using step timing and location adjustment on the humanoid robot, Atlas. In *2017 IEEE/RSJ International Conference on Intelligent Robots and Systems (IROS)*, pages 667–673. IEEE.
- Haldane, D. W., Plecnik, M. M., Yim, J. K., and Fearing, R. S. (2016). Robotic vertical jumping agility via series-elastic power modulation. *Science Robotics*, 1(1).
- Harmonic Drive (2020). Harmonic Drive CSF-2A Component Set. <https://www.harmonicdrive.net/products/component-sets/cup-type/csf-2a>. Accessed: 2020-04-02.
- Haueisen, B. M. (2011). *Investigation of an Articulated Spine in a Quadruped Robotic System*. PhD thesis, University of Michigan.
- Hokuyo (2020). Hokuyo UTM-30LX-EW. <https://www.hokuyo-aut.jp/search/single.php?serial=170>. Accessed: 2020-03-31.
- Hubicki, C., Grimes, J., Jones, M., Renjewski, D., Spröwitz, A., Abate, A., and Hurst, J. (2016). ATRIAS: Design and validation of a tether-free 3D-capable spring-mass bipedal robot. *The International Journal of Robotics Research*, 35(12):1497–1521. doi: 10.1177/0278364916648388.
- Hutter, M., Gehring, C., Jud, D., Lauber, A., Bellicoso, C. D., Tsounis, V., Hwangbo, J., Bodie, K., Fankhauser, P., Bloesch, M., et al. (2016). ANYmal-a highly mobile and dynamic quadrupedal robot. In *2016 IEEE/RSJ International Conference on Intelligent Robots and Systems (IROS)*, pages 38–44. IEEE.

- Jafari, A., Tsagarakis, N. G., and Caldwell, D. G. (2011). A novel intrinsically energy efficient actuator with adjustable stiffness (AwAS). *IEEE/ASME transactions on mechatronics*, 18(1):355–365. doi: 10.1109/TMECH.2011.2177098.
- Jansen, D. and Buttner, H. (2004). Real-time Ethernet: the EtherCAT solution. *Computing and Control Engineering*, 15(1):16–21.
- Katz, B. G. (2018). *A low cost modular actuator for dynamic robots*. PhD thesis, Massachusetts Institute of Technology.
- Kenneally, G., De, A., and Koditschek, D. E. (2016). Design principles for a family of direct-drive legged robots. *IEEE Robotics and Automation Letters*, 1(2):900–907. doi: 10.1109/LRA.2016.2528294.
- Klein, C. A. and Briggs, R. L. (1980). Use of active compliance in the control of legged vehicles. *IEEE Transactions on Systems, Man, and Cybernetics*, 10(7):393–400.
- Koenig, S. and Likhachev, M. (2002). D\* lite. In *Eighteenth national conference on Artificial intelligence*, pages 476–483.
- Krause, M., Engelsberger, J., Wieber, P.-B., and Ott, C. (2012). Stabilization of the capture point dynamics for bipedal walking based on model predictive control. *IFAC Proceedings Volumes*, 45(22):165 – 171. doi: 10.3182/20120905-3-HR-2030.00165.
- Krüsi, P., Furgale, P., Bosse, M., and Siegwart, R. (2017). Driving on point clouds: Motion planning, trajectory optimization, and terrain assessment in generic nonplanar environments. *Journal of Field Robotics*, 34(5):940–984. doi: 10.1002/rob.21700.
- Mattila, J. and Virvalo, T. (2000). Energy-efficient motion control of a hydraulic manipulator. In *Proceedings 2000 ICRA. Millennium Conference. IEEE International Conference on Robotics and Automation. Symposia Proceedings (Cat. No. 00CH37065)*, volume 3, pages 3000–3006. IEEE.
- Murray, R. M., Li, Z., Sastry, S. S., and Sastry, S. S. (1994). *A mathematical introduction to robotic manipulation*. CRC Press.
- Nicholson, J. V., Gart, S., Pusey, J., and Clark, J. E. (2020). Evaluating the efficacy of parallel elastic actuators on high-speed, variable stiffness running. In *2020 IEEE/RSJ International Conference on Intelligent Robots and Systems (IROS)*. IEEE.
- Ott, C., Mukherjee, R., and Nakamura, Y. (2015). A hybrid system framework for unified impedance and admittance control. *Journal of Intelligent & Robotic Systems*, 78(3-4):359–375. doi: 10.1007/s10846-014-0082-1.
- Park, H.-W., Chuah, M. Y., and Kim, S. (2014). Quadruped bounding control with variable duty cycle via vertical impulse scaling. In *2014 IEEE/RSJ International Conference on Intelligent Robots and Systems*, pages 3245–3252. IEEE.
- Park, H.-W., Wensing, P. M., and Kim, S. (2017). High-speed bounding with the MIT cheetah 2: Control design and experiments. *The International Journal of Robotics Research*, 36(2):167–192.
- Potter, S., Jackowski, Z., and Young, A. (2019). Screw Actuator for a Legged Robot. US Patent 10,253,855.
- Pratt, G. A. and Williamson, M. M. (1995). Series elastic actuators. In *Proceedings 1995 IEEE/RSJ International Conference on Intelligent Robots and Systems. Human Robot Interaction and Cooperative Robots*, volume 1, pages 399–406. IEEE.
- Pratt, J., Carff, J., Drakunov, S., and Goswami, A. (2006). Capture point: A step toward humanoid push recovery. In *2006 6th IEEE-RAS international conference on humanoid robots*, pages 200–207. IEEE.
- Raibert, M., Blankespoor, K., Nelson, G., and Playter, R. (2008). BigDog, the rough-terrain quadruped robot. *IFAC Proceedings Volumes*, 41(2):10822–10825.
- Robinson, D. W., Pratt, J. E., Paluska, D. J., and Pratt, G. A. (1999). Series elastic actuator development for a biomimetic walking robot. In *1999 IEEE/ASME International Conference on Advanced Intelligent Mechatronics (Cat. No. 99TH8399)*, pages 561–568. IEEE.
- Semini, C., Goldsmith, J., Rehman, B. U., Frigerio, M., Barasuol, V., Focchi, M., and Caldwell, D. G. (2015). Design overview of the hydraulic quadruped robots HyQ2MAX and HyQ2CENTAUR. In *The Fourteenth Scandinavian International Conference on Fluid Power*, pages 20–22.
- Seok, S., Wang, A., Chuah, M. Y., Otten, D., Lang, J., and Kim, S. (2013). Design principles for highly efficient quadrupeds and implementation on the MIT Cheetah robot. In *2013 IEEE International Conference on Robotics and Automation*, pages 3307–3312. IEEE.
- Seok, S., Wang, A., Otten, D., and Kim, S. (2012). Actuator design for high force proprioceptive control in fast legged locomotion. In *2012 IEEE/RSJ International Conference on Intelligent Robots and Systems*, pages 1970–1975. IEEE.

- Spröwitz, A., Tuleu, A., Vespignani, M., Ajallooeian, M., Badri, E., and Ijspeert, A. J. (2013). Towards dynamic trot gait locomotion: Design, control, and experiments with Cheetah-cub, a compliant quadruped robot. *The International Journal of Robotics Research*, 32(8):932–950. doi: 10.1177/0278364913489205.
- Takenaka, T., Matsumoto, T., and Yoshiike, T. (2009). Real time motion generation and control for biped robot -1st report: Walking gait pattern generation. In *IEEE/RSJ International Conference on Intelligent Robots and Systems (IROS)*, pages 1084–1091.
- Thrun, S. (2002). Probabilistic robotics. *Communications of the ACM*, 45(3):52–57.
- Urata, J., Nakanishi, Y., Okada, K., and Inaba, M. (2010). Design of High Torque and High Speed Leg Module for High Power Humanoid. In *2010 IEEE/RSJ International Conference on Intelligent Robots and Systems*. IEEE.
- Waymo (2020). Waymo Laser Bear Honeycomb. <https://waymo.com/lidar/>. Accessed: 2020-03-31.
- Wensing, P. M., Wang, A., Seok, S., Otten, D., Lang, J., and Kim, S. (2017). Proprioceptive actuator design in the MIT Cheetah: Impact mitigation and high-bandwidth physical interaction for dynamic legged robots. *IEEE Transactions on Robotics*, 33(3):509–522. doi: 10.1109/TRO.2016.2640183.

**How to cite this article:** Jasper, J., Kourchians, A., Gonzalez, M., Emanuel, B., Nicholson, J., McCutcheon, G., Austin, M., Kozłowski, M., Holmes, E., Hegeman, R., McCrory, S., Zeher, M., Handelman, D., Griffin, R., Karumanchi, S., Hubicki, C., Kennedy, B., Clark, J., Pratt, J., Patel, D., & Pusey, J. (2022). Lessons learned from two iterations of LLAMA, an electrically powered, dynamic quadruped robot. *Field Robotics*, 2, 325–355.

**Publisher's Note:** Field Robotics does not accept any legal responsibility for errors, omissions or claims and does not provide any warranty, express or implied, with respect to information published in this article.